Alma Mater Studiorum · University of Bologna

School of Science
Department of Physics and Astronomy
Master Degree in Physics

Small polarons in Spin-Orbit coupled osmates

Supervisor:
Prof. Cesare Franchini

Co-supervisor:
Dr. Dario Fiore Mosca

Submitted by:
Lorenzo Celiberti

Academic Year 2020/2021

Abstract

Small polarons (SP) have been thoroughly investigated in $3d$ transition metal oxides and they have been found to play a crucial role in physical phenomena such as charge transport, colossal magnetoresistance and surface reactivity [1]. However, our knowledge about these quasi-particles in $5d$ systems remains very limited, since the more delocalised nature of the $5d$ orbitals reduces the strength of the Electronic Correlation (EC), making SP formation in these compounds rather unexpected. Nevertheless, the Spin-Orbit coupled Dirac-Mott insulator Ba_2NaOsO_6 (BNOO) represents a good candidate for enabling polaron formation in a relativistic background, due to the relatively large EC ($U \sim 3\,\mathrm{eV}$) and Jahn-Teller activity [2]. Moreover, anomalous peaks in Nuclear Magnetic Resonance (NMR) spectroscopy experiments suggest the presence of thermally activated SP dynamics when BNOO is doped with Ca atoms. We investigate SP formation in BNOO both from an electronic and structural point of view by means of fully relativistic first principles calculations. Our numerical simulations predict a stable SP ground state and agree on the value of 810 K for the dynamical process peak found by NMR experiments.

Abstract

I polaroni piccoli (PP) sono stati intensivamente studiati negli ossidi contenti metalli di tansizione con orbitali $3d$ e si sono rivelati cruciali nel determinare diverse proprietà fisiche di questi materiali, come trasporto di carica, resistenza magnetica colossale e reattivitá di superficie [1]. Tuttavia la nostra conoscenza riguardo queste quasi-particelle in sistemi $5d$ é tutt'ora molto limitata. Infatti, la natura più delocalizzata degli orbitali $5d$ riduce l'intensità della correlazione elettronica (CE) e rende di conseguenza la formazione di PP piuttosto improbabile. Ad ogni modo, l'isolante di Dirac-Mott Ba_2NaOsO_6 (BNOO) rappresenta un buon candidato per l'eventuale formazione di PP in un contesto relativistico, grazie al forte accoppiamento Spin-Orbita, la relativamente grande CE ($U \sim 3\,\mathrm{eV}$) e l'attività Jahn-Teller [2]. Per di più, picchi anomali registrati in esperimenti di spettroscopia a risonanza magnetica nucleare (NMR) suggeriscono la presenza di un moto di PP indotto termicamente, quando BNOO viene drogato con Ca. In questo lavoro investighiamo quindi la formazione di PP in BNOO sia da un punto di vista delle deformazioni strutturali che elettronico, attravverso calcoli numerici in uno schema relativistico che non coinvolge parametri empirici (first principles). Le nostre simulazioni numeriche confermano l'ipotesi dell'esistenza di una configurazione polaronica stabile e concordano nel valore di $\sim 810\,\mathrm{K}$ per la posizione del picco anomalo nello spettro NMR.

Contents

List of Figures

Acronyms

BNOO Ba_2NaOsO_6

cAFM canted anti-ferromagnetic

CF Crystal Field

DFT Density Functional Theory

DMI Dirac-Mott Insulator

DOS Density Of States

EC Electronic Correlation

EHAM Emin-Holstein-Austin-Mott

GGA Generalised Gradient Approximation

HK Hohenberg-Kohn

JT Jahn-Teller

LDA Local Density Approximation

LIS Linear Interpolation Scheme

LSDA Local Spin-Density Approximation

MF Mean Field

MIT Metal-Insulator Transition

NEB Nudged Elastic Band

NMR Nuclear Magnetic Resonance

PAW Projector Augmented Wave

SOC Spin-Orbit coupling

SP Small Polaron

TB Tight Binding

TM Transition Metal

TMO Transition Metal Oxide

UHF Unrestricted Hartree-Fock

VASP Vienna Ab-initio Simulation Package

VSC Vienna Scientific Cluster

Introduction

Small Polarons (SPs) are localized charges trapped by the potential well that they induce in the crystal lattice, by displacing the surrounding ions. They are hence self-trapped quasiparticles that can form even in perfect crystals, as was first suggested by Lev Landau [1]. Their impact on the electronic, structural and magnetic properties of crystalline materials has been widely investigated in $3d$ Transition Metal Oxides (TMOs), where Electronic Correlation (EC) plays a significant role in localizing such states [1, 3]. However, very little is known about these quasiparticles in $5d$ materials, where the more delocalised nature of these orbitals reduces the strength of EC. A consequence of the EC weakness is that the Mott insulating phase, characteristic of many $3d$ TMOs, hardly set in. Nevertheless there are special cases where strong Spin-Orbit coupling (SOC) can conspire with EC in order to open an insulating gap, as it has been found in the $5d$ TMO Sr_2IrO_4 [4–6]. Materials showing this peculiar phase are now known as *relativistic* or Dirac-Mott Insulators (DMIs) and among them the double perovskite Ba_2NaOsO_6 (BNOO) [7, 8] shows a particular balance between EC, strong SOC ($\lambda \sim 0.5\,\mathrm{eV}$), Jahn-Teller (JT) and magnetic interactions that makes it at the same time an intriguing and difficult system to study. As an example of the complexity that can emerge from the interplay of all these interactions, let's consider that Nuclear Magnetic Resonance (NMR) experiments [8] and first principles calculations [2] showed that BNOO is a magnetic oxide with an exotic canted anti-ferromagnetic (cAFM) ordering that is, moreover, sustained by JT distortions.

Another fact that makes BNOO particular interesting is its behaviour under electron doping, when Na is partially replaced by non-isovalent Ca. X-ray diffraction experiments showed that in this way we obtain an alloy $Ba_2Na_{1-x}Ca_xOsO_6$, in which the additional charge is transferred from the Ca to the Os atoms and the latter go from a formal valece of +7 in BNOO to +6 in Ba_2CaOsO_6, which is still a DMI [9]. But for other TMOs and

especially for the protoypical DMI Sr_2IrO_4, the cation substitution process usually leads to an Insulator-Metal transition [10–13]. Since BNOO has also a higher EC ($U \sim 3\,\text{eV}$) with respect to other DMIs, we conjectured that the chemical doping in this material is accompanied by SP formation, in such a way that the excess charge remains trapped all along the process, preventing the transition. If this may still sound rather speculative, earlier this year spin-lattice and spin-spin relaxation measurements, performed by using ^{23}Na NMR spectroscopy, showed peaks typical of thermally activated SP hopping, similar to those observed in lanthanum manganites [14]. Even though these results are yet to be published, they strongly suggest the presence of SP dynamics at all Ca concentrations between 12.5% and 90%.

We thereby set the stage for the exploration of SP formation in $Ba_2Na_{1-x}Ca_xOsO_6$ by calculating from first principles some quantities that could potentially bare the footprints of SPs. We start by spending some words more, in chapter 1, on the physical concepts that we rapidly mentioned above, as EC and SOC, and by presenting the core ideas that make it possible to perform calculations on such complex systems in chapter 2. Then we will give a deeper presentation of the double perovskite Ba_2NaOsO_6 in chapter 3 so that we can eventually go through the results of the simulations in chapter 4 and answer to the question of whether SPs do actually form in this material or not.

All the calculations in this work have been conducted using the Vienna Ab-initio Simulation Package (VASP), developed by the group of Georg Kresse at the University of Vienna [15–17], on the cluster at the Vienna Scientific Cluster (VSC) facility. Crystal structure and charge density images have been produced using the VESTA software [18], whereas band structure data have been extracted from VASP output using the Python Materials Genomics (pymatgen) library [19].

Chapter 1

Physical background

TMOs represent a vast class of materials characterised by strong EC. This makes ordinary band theory unable to describe their electronic structure and leads to the formation of new phases, such as that of Mott insulators and a variety of exotically ordered magnets [20]. Along with EC, Crystal Field (CF), JT distortions and the SOC interaction can in some cases be crucial in the understanding of TMOs' physics [21–23]. Moreover, these compounds are the playground for intriguing phenomena such high-T_c superconductivity and colossal magnetoresistance [24–26].

Among the variety of phenomena taking place in this class of materials, polarons formation is one that has attracted particular attention in the last century. The last decades in particular have seen a boost in this field of physical research thanks to the development of computational techniques and facilities capable of attacking the complexity of the electron-phonon interaction problem [1].

We shall briefly introduce in the following sections the main concepts relevant to TMOs' and polarons' physics, within the scope of our work. Each section in this chapter would indeed deserve and has been treated in whole books.

1.1 Electronic Correlation

The starting point for the study of crystalline materials is the band theory, developed in the first half of the twentieth century (see *e.g.* [27]). In its simplest formulation, electrons can be considered as a gas of non-interacting particles, which only interact with the periodic potential arising from the (fixed) lattice of ions. Although this picture allows us to understand some qualitative features of crystals, it clearly consists of a rough approximation. This is particularly true in those cases where the electron-electron interaction is more strong, such as in TMOs. One severely unphysical prediction of band theory is that if a material has an odd number of electrons in the primitive cell, then it is a conductor, no matter how large the distance between the atoms is. This is a consequence of the Born-von Karman periodic boundary conditions and the Bloch theorem [27], which predict that each band contains N wave vectors, where N is the number of sites in the whole crystal. Therefore, each band contains $2N$ states, due to spin degeneracy. This implies that in the case of an odd number of electrons in the primitive cell, there must be a half-filled band and hence the material is a conductor. The distance between the atoms in the crystal does not play any role in these considerations.

To delve further into this problem and introduce some notation that will be useful later on, let's analyse the problem in the Tight Binding (TB) approximation. Within this scheme we take the electron wavefunction as a linear combination of atomic (localised) wavefunctions ϕ_n (another choice is to use Wannier functions [27]) and assume that the external potential $V(r)$ due to the lattice can be written as the sum of local functions $U(r)$ centered at each site

$$V(r) = \sum_n U(r - na) \tag{1.1}$$

If we consider a one dimensional chain of atoms with a single valence electron and non-degenerate levels, the TB Hamiltonian can be written in the second quantisation formalism as

$$H = -t \sum_{\langle i,j\rangle,\sigma} c^\dagger_{i\sigma} c_{j\sigma} + \text{h.c.} \tag{1.2}$$

where the product of the fermionic creation and annihilation operators, $c^\dagger_{i\sigma}$ and $c_{j\sigma}$ respectively, gives the hopping of an electron with spin σ from site j to site i. The hopping constant t quantifies the probability for this process to take place and decreases

with increasing lattice constant a. This quantity comes indeed from the hopping integral

$$t_{ij} = \int \mathrm{d}r\ \phi^*(r - ia)U(r - ia)\phi(r - ja) \tag{1.3}$$

if we assume that its value does not depend on the particular pair of nearest neighbours considered. Going form the localised to the Bloch basis, we can calculate the dispersion relation of Equation 1.2 obtaining

$$\epsilon(k) = -2t \cos ka \tag{1.4}$$

which is a half-filled band, with bandwidth $W = 4t$ and therefore our chain has a metallic behaviour. In the limit of large lattice constant, *i.e.* large inter-atomic separation, the hopping constant goes to zero and the band gets narrower, but it remains half-filled throughout the whole limit process [20]. In simpler words, we could imagine a chain with atoms one kilometer apart and it will still be a metal according to band theory, even though we are far beyond the typical distance for bonding to occur.

Let's now introduce electron-electron interaction. The simplest consideration that we can do is to take into account the coulombic repulsion experienced by a hopping electron, due to electrons at the arrival site. If an orbital already has an electron, an energy amount U must be provided in order to put another electron in it. Moreover, the second particle must have opposite spin with respect to the first, due to the Pauli principle. These requirements are satisfied if we insert a second term into our Hamiltonian, obtaining

$$H = -t \sum_{\langle i,j\rangle,\sigma} c^\dagger_{i\sigma} c_{j\sigma} + \text{h.c.} + U \sum_i n_{i\uparrow} n_{i\downarrow} \tag{1.5}$$

which describes the so-called *Hubbard model*.

When an electron jumps in another site we end up with an empty (*hole*) and a completely filled orbital, respectively at the initial and final sites. These exicitations now can hop around in the crystal and form bands, according to Equation 1.2. They occupy the lowest state in this band, which has energy $-2t$. Thus in forming this conductive state we gained an energy equal to W and payed U.

From these considerations we can now argue that, when $U \gtrsim W$, there is no energy gain in the formation of the excited state and the electrons stay localized at their sites,

even though from a band-theory picture the material would have been a metal. This particular state of matter is called a *Mott insulator* and the Hubbard model is the simplest one capable to describe it, along with the related Metal-Insulator Transition (MIT).

1.2 Spin-Orbit Coupling

We make now a little digression into atomic physics in order to introduce the concept of Spin-Orbit coupling (SOC), which along with EC is responsible for many peculiar properties of compounds containing heavy atoms, such as the establishment of the Dirac-Mott phase in Sr_2IrO_4 [22]. This coupling between spin and orbital degrees of freedom is a relativistic effect that can be understood within the framework of the Dirac equation for a spin 1/2 particle:

$$i\hbar\frac{\partial\Psi}{\partial t} = c\alpha\cdot\mathbf{p}\Psi + mc^2\beta\Psi \tag{1.6}$$

Here the particle is described by a four dimensional spinor Ψ, whose components represent the two spin degrees of freedom of the particle itself and those of its antiparticle. The quantities $\alpha = (\alpha_1, \alpha_2, \alpha_3)$ and β are matrices defined as

$$\alpha_k = \begin{pmatrix} 0 & \sigma_k \\ \sigma_k & 0 \end{pmatrix} \qquad \beta = \begin{pmatrix} \mathbb{1} & 0 \\ 0 & \mathbb{1} \end{pmatrix} \tag{1.7}$$

where σ_k are the Pauli matrices. The momentum operator $\mathbf{p}$ in Equation 1.6 is defined as usual $\mathbf{p} = -i\hbar\nabla$. Let's consider a stationary solution $\Psi = \psi(\mathbf{r})\exp(-iEt/\hbar)$. If we split the four component spinor ψ as

$$\psi(\mathbf{r}) = \begin{pmatrix} \psi_A(\mathbf{r}) \\ \psi_B(\mathbf{r}) \end{pmatrix} \tag{1.8}$$

then, from Equation 1.6, we get the coupled equations for the two-components spinors ψ_A and ψ_B

$$E\psi_A - c\boldsymbol{\sigma}\cdot(\mathbf{p} - q\mathbf{A})\psi_B + \big(q\phi + mc^2\big)\psi_A = 0, \tag{1.9a}$$

$$E\psi_B - c\boldsymbol{\sigma}\cdot(\mathbf{p} - q\mathbf{A})\psi_A + \big(q\phi - mc^2\big)\psi_B = 0 \tag{1.9b}$$

where the coupling with an electromagnetic field $(\mathbf{A}, \phi)$ has been taken into account.

Now, for an electron in an atom we can take $\mathbf{A} = 0$ and ϕ to be spherically symmetric, so that we can write $q\phi(\mathbf{x}) = U(r)$. Equation 1.9a and Equation 1.9b become

$$E\psi_A - c\boldsymbol{\sigma} \cdot \mathbf{p}\ \psi_B - \big(U - mc^2\big)\psi_A = 0, \tag{1.10a}$$
$$E\psi_B - c\boldsymbol{\sigma} \cdot \mathbf{p}\ \psi_A - \big(U + mc^2\big)\psi_B = 0 \tag{1.10b}$$

Writing the energy as $E = E' + mc^2$, from Equation 1.10b we get

$$\psi_B = \frac{1}{E' + mc^2 - U(r)}\boldsymbol{\sigma} \cdot \mathbf{p}\ \psi_A \tag{1.11}$$

In a non-relativistic regime the kinetic term is much smaller than the mass energy, we can thus write

$$\psi_B = \frac{1}{2mc}\left[1 - \frac{E' - U(r)}{2mc^2}\right]\boldsymbol{\sigma} \cdot \mathbf{p}\ \psi_A \tag{1.12}$$

By inserting this expression into Equation 1.10a we get

$$E'\psi_A - \frac{1}{2m}\mathbf{p}^2\left[1 - \frac{E' - U(r)}{2mc^2}\right]\psi_A - U(r)\psi_A - \frac{1}{4m^2c^2}(\boldsymbol{\sigma} \cdot \mathbf{p})U(r)(\boldsymbol{\sigma} \cdot \mathbf{p})\psi_A = 0 \tag{1.13}$$

Using the identity

$$(\boldsymbol{\sigma} \cdot \mathbf{A})(\boldsymbol{\sigma} \cdot \mathbf{B}) = \mathbf{A} \cdot \mathbf{B} + i\sigma \cdot (\mathbf{A} \times \mathbf{B}) \tag{1.14}$$

we get

$$\begin{aligned}(\boldsymbol{\sigma} \cdot \mathbf{p})U(r)(\boldsymbol{\sigma} \cdot \mathbf{p})\psi_A &= -i\hbar(\boldsymbol{\sigma} \cdot \boldsymbol{\nabla}U)(\boldsymbol{\sigma} \cdot \mathbf{p})\psi_A \\ &= -\hbar^2\boldsymbol{\nabla}U \cdot \boldsymbol{\nabla}\psi_A + \hbar\ \frac{1}{r}\frac{\mathrm{d}U}{\mathrm{d}r}\boldsymbol{\sigma} \cdot (\mathbf{r} \times \mathbf{p})\psi_A\end{aligned} \tag{1.15}$$

where the first term in the last equality gives rise to the so called *Darwin term* [28], whereas the last one is the SOC one. Recalling that the orbital angular momentum is $\mathbf{L} = \mathbf{r} \times \mathbf{p}$ and the Pauli operator consists basically of the spin operator $\mathbf{S} = \hbar/2\boldsymbol{\sigma}$, we get

$$H_{SOC} = -\frac{1}{2m^2c^2}\frac{1}{r}\frac{\mathrm{d}U}{\mathrm{d}r}\mathbf{S} \cdot \mathbf{L} \equiv \xi(r)\mathbf{S} \cdot \mathbf{L} \tag{1.16}$$

Let's rewrite the Hamiltonian for the Hydrogen atom neglecting the Darwin term, which is $\mathcal{O}(v^2/c^2)$, and the kinetic energy shift coming from the second term in the sqare bracket

of Equation 1.13 as

$$H = \frac{1}{2}\mathbf{p}^2 + U(r) + \xi(r)\mathbf{S}\cdot\mathbf{L} \tag{1.17}$$

where atomic units are assumed. Using the commutation relation of the angular momentum operator we can prove that this Hamiltonian commutes neither with the orbital angular momentum $\mathbf{L}$ nor with the spin $\mathbf{S}$, we have indeed

$$[\mathbf{S}\cdot\mathbf{L}, L_k] = i\hbar(\mathbf{L}\times\mathbf{S})_k = -[\mathbf{S}\cdot\mathbf{L}, S_k] \tag{1.18}$$

Therefore, the orbital angular momentum is not a conserved quantity anymore and we cannot use the magnetic quantum number l_z, related to the azimuthal component of $\mathbf{L}$, to describe our system. From Equation 1.18, on the other hand, we can easily see that the SOC Hamiltonian commutes instead with the *total angular momentum* $\mathbf{J} = \mathbf{L} + \mathbf{S}$. Since the modulus squared of orbital angular momentum $\mathbf{L}^2$ and that of the spin $\mathbf{S}^2$ are still conserved quantity we can go from the original basis $|l, l_z, s, s_z\rangle$ to $|j, j_z, l, s\rangle$ and use the total angular momentum j and its z-component to replace l_z and s_z. The transformation matrix that connects these two basis is given by the Clebsch-Gordan theorem [28]. Noticing that

$$\mathbf{S}\cdot\mathbf{L} = \frac{1}{2}\big(J^2 - L^2 - S^2\big) \tag{1.19}$$

we can calculate the expectation value of the SOC Hamiltonian on the new basis $|j, j_z, l, s\rangle$:

$$\langle j, j_z, l, s|H_{SOC}|j, j_z, l, s\rangle = \langle\xi(r)\rangle\,\frac{j(j+1) - l(l+1) - 3/4}{2} \tag{1.20}$$

from which we see that the original $(2l+1)$-degenerate level is split into two levels with total angular momentum $j = |l - 1/2|$ and $j = l + 1/2$ except for the s-orbitals.

When we consider atoms with more than one electron, correlation effects must be taken into account. Within a Mean Field (MF) approach we can write the atomic Hamiltonian as the sum of an independent-particle term H_{MF}, a correction due to correlation H_{corr} and the spin-orbit contribution H_{SOC}, which now looks like

$$H_{SOC} = \sum_i \xi_i(r_i)\mathbf{S}_i\cdot\mathbf{L}_i \tag{1.21}$$

We can distinguish between two perturbative regimes known as the *LS-coupling* (or Russell-Saunders) and the *jj-coupling* regimes. They are extreme situations where we can consider the SOC interaction ($\langle H_{corr}\rangle \gg \langle H_{SOC}\rangle$) or the correlation effect ($\langle H_{SOC}\rangle \gg \langle H_{corr}\rangle$) as a perturbation. The jj-coupling scheme is usually applied only to those elements with very strong SOC, namely $4f$ and $5f$ compounds, whereas the LS-scheme works quite well for $3d$ and $4d$ atoms. The case of $5d$ constitutes an intermediate situation where the perturbative approach is not that accurate and we must therefore turn to different methods [20].

1.3 Crystal Field

We discussed so far the role of SOC in isolated atoms, where the electronic states were characterised by the spin S, the orbital angular momentum L and the total angular momentum J quantum numbers. Now we want to move our discussion to crystals. Here we have to consider that atoms are not in an isotropic environment anymore and therefore the electrons move in a potential field that is not spherically symmetric. For this reason, we cannot in principle describe electronic terms with the orbital L and total angular momentum J quantum numbers, but should use instead the representations of the point group of the crystal. However, we can introduce effective angular momenta, which allow to discuss, at least qualitatively, localised states in crystals with the same language of atomic physics [20].

In order to elucidate the role of the Crystal Field (CF), namely the anisotropic field felt by the electrons in a crystal, we shall consider a Transition Metal (TM) atom surrounded by oxygen atoms placed at the corners of an octahedron, as depicted in Figure 1.3.1. From group theoretical arguments (see *e.g.* [20] and references therein) we find out that the five degenerate d orbitals are split into a doublet e_g and a low lying energy t_{2g}. The energy separation Δ_{CF} between these two levels is called CF splitting. Physically this can be understood by inspecting the orbital character of the e_g and t_{2g} levels, namely by observing the spatial distribution of the spherical harmonics $|l^z\rangle$ that

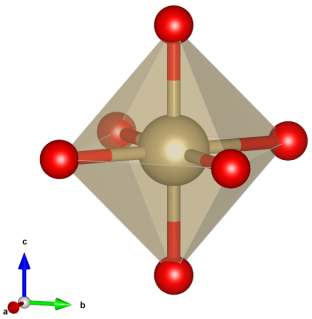

Figure 1.3.1: Octahedrally coordinated TM atom (brown sphere). The figure has been adapted from that of the unit cell of BNOO used in the calculations and therefore the red spheres are oxygen atoms. Nevertheless, they could have been a general anion.

make up these states. If we choose a real combination of the basis functions $|l^z\rangle$, we get

$$e_g : \begin{cases} |z^2\rangle = |0\rangle \sim \frac{1}{\sqrt{6}}(3z^2 - r^2) \\ |x^2 - y^2\rangle = \frac{1}{\sqrt{2}}(|2\rangle + |-2\rangle) \sim \frac{1}{\sqrt{2}}(x^2 - y^2) \end{cases} \tag{1.22}$$

$$t_{2g} : \begin{cases} |xy\rangle = -\frac{i}{\sqrt{2}}(|2\rangle - |-2\rangle) \sim \sqrt{3}xy \\ |xz\rangle = -\frac{1}{\sqrt{2}}(|1\rangle - |-1\rangle) \sim \sqrt{3}xz \\ |yz\rangle = \frac{i}{\sqrt{2}}(|1\rangle + |-1\rangle) \sim \sqrt{3}yz \end{cases} \tag{1.23}$$

It turns out that e_g orbitals have lobes pointing directly at lobes of the p orbitals of the neighbouring oxygens, whereas t_{2g} orbitals point at the space between the oxygen atoms (see Figure 1.3.2). Therefore, e_g electrons feel a stronger Coulomb repulsion than t_{2g} ones, due to the charge distribution of the oxygen atoms. This argument gives rise to the *point charge contribution* [20].

Another effect to be considered in the determination of the CF splitting is the *covalency*, namely the degree of overlap of the d orbitals of the TM atom with the p orbitals of the oxygen ones. The larger the overlap, the higher is indeed the hopping probability between the two sites and hence the kinetic energy. By looking once again at Figure 1.3.2, it is clear that e_g orbitals point directly at lobes of the oxygen p orbitals, whereas t_{2g} orbitals end up in regions with low p density. This implies that hopping elements for e_g

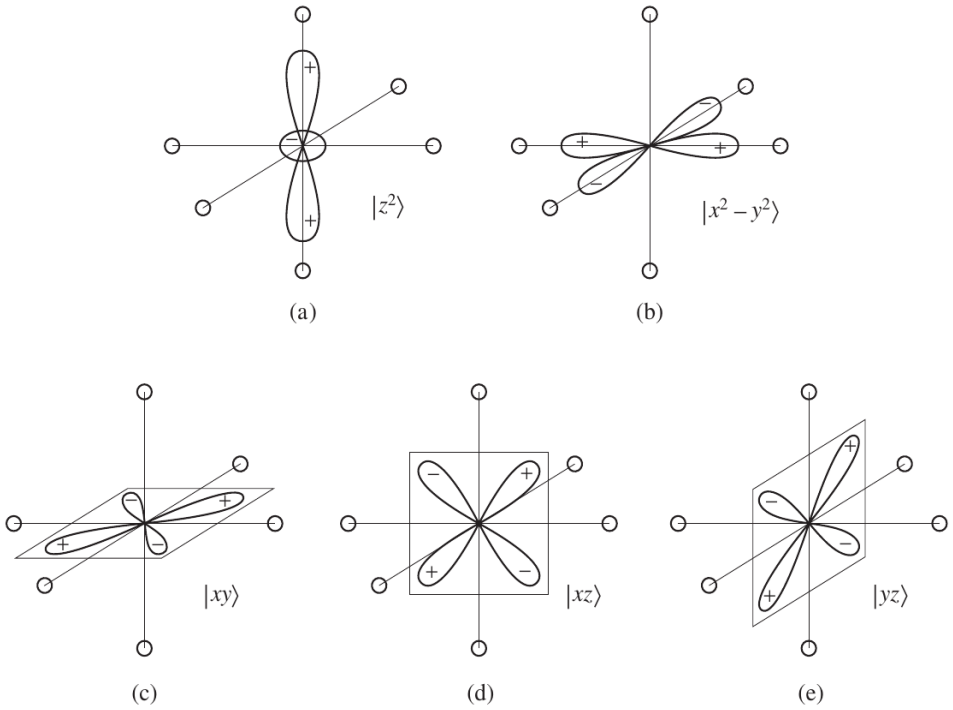

Figure 1.3.2: Charge distribution of the d-orbitals. (a) and (b) in the first row make e_g oritals in an octahedrally coordinated compound, whereas (c), (d) and (e) give rise to the t_{2g} ones. Picture taken from Khomskii [20].

are larger than those for t_{2g} and, therefore, e_g levels are shifted toward higher energies.

Since the triplet t_{2g} states are orbitally degenerate, we can map them into an effective orbital angular momentum $\tilde{l} = 1$ eigenstates and correspondingly introduce an effective total angular momentum $\tilde{J} = \left|S - \tilde{l}\right|, \ldots, S+\tilde{l}$ [20, 29]. By using these effective momenta, SOC splitting within the CF scheme can be qualitatively discussed as in the case of isolated atoms[1].

Another critical consideration to do is that ions are actually not fixed and a rearrangement of their configuration is indeed a quite common situation [20, 29, 30]. In order to qualitatively understand the implications of such a process, let's consider a tetragonal elongation of our octahedron of Figure 1.3.1:

$$z \to z + 2\delta \qquad x \to x - \delta \qquad y \to y - \delta \tag{1.24}$$

[1]In our case of octahedral coordination actually, we should take $\tilde{l} = -1$ in order to recover the same ordering of SOC splitted $l = 1$ levels in an isolated atom. For further details see *e.g.* [20].

with δ a positive small deformation. By pushing the oxygen atoms away from the TM, both Coulomb repulsion and overlap of $|z^2\rangle$ are reduced. On the other hand those of $|x^2 - y^2\rangle$ are increased, so that eventually e_g orbitals split. The same argument applies for t_{2g} orbitals as well.

Distortions like those mentioned above occur whenever there is an orbital denegeracy besides the spin (Kramers) degeneracy, according to the *Jahn-Teller theorem* [30]. We won't discuss the interesting physics of the JT effect, because we didn't analyse in details the role of JT in our work. However, the splitting arising from JT distortions may compete or play together with that of SOC [21]. This interplay has a crucial role for instance in the determination of the magnetic ground state of BNOO [2] and a deeper investigation of JT physics in BNCOO may constitute an interesting continuation of this study.

1.4 Polarons

In the previous section we mentioned the JT theorem which connects the electronic degrees of freedom to those of the lattice. It turns out however that this is not the only possible way in which electrons and phonons, the quanta of lattice vibrations, can interact with each other. In 1933 Lev Landau suggested that electron-phonon interactions could lead to the self-trapping of charge carriers (electrons or hole) even in perfect crystals, resulting in the formation of a quasiparticle, namely the *polaron*. An electron (hole) can distort the crystal lattice around itself via Coulomb interaction. The ions thus displaced produce in turn a polarisation field characterised by a potential well that, if deep enough, may trap the charge carrier that was originally responsible for the field itself. This situation is pictorially represented in Figure 1.4.1. The name polaron, evocative of the process leading to the formation of these quasiparticles, was coined afterwards, in 1946, by Solomon Pekar, who also proposed a first model based on the interaction of free electrons moving in a ionic lattice, approximated as a polarizable continuum [1, 31].

Further developments of the concept came in the '50s with the elaboration of effective field theories by Herbert Fröhlich [33] and Theodore Holstein [34]. Their theories describe two limiting cases: the weak limit of the electron-phonon coupling gives the Fröhlich Hamiltonian, whereas the strong coupling is represented by the Holstein's. The stronger is the coupling, the smaller is the spatial extension of the quasiparticle. Thus the Fröhlich

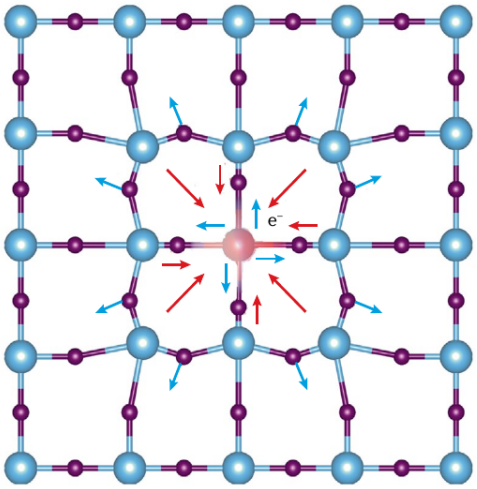

Figure 1.4.1: Pictorial representation of a polaron as a self-trapped charge in a crystal. The figure has been taken from Natanzon *et al.* [32].

polaron is also one whose charge is distributed over many lattice sites and we speak of *large polaron*. On the other hand, the Holstein polaron is called *small polaron*, because the polaronic radius is smaller than the lattice parameter. The main differences between large and small polarons are summarised in Table 1.1.

Large Polaron	Small Polaron
Polaron radius $\gg$ lattice parameter	Polaron radius $\sim$ lattice parameter
Shallow state ($\sim 10\,\text{meV}$ below CBM)	In-gap state ($\sim 1\,\text{eV}$ below CBM)
Coherent motion (scattered occasionally by phonons)	Incoherent motion (assisted by phonons)
Mobility $\mu \gg 1\,\text{cm}^2/\text{Vs}$	Mobility $\mu \ll 1\,\text{cm}^2/\text{Vs}$
Decreasing mobility with increasing temperature	Increaing mobility with increasing temperature

Table 1.1: Relevant characteristics of large and small polarons. This table has been adapted from [35].

From an electronic point of view large polarons are identified by shallow states, usually few tens of meV below the conduction band maximum (CBM), whereas small polarons are deep in-gap states, around 1 eV below CBM [35].

A crucial feature of polarons is their mobility. Besides that polarons do not need defects to form, they are also different from defect states beacause of their ability to

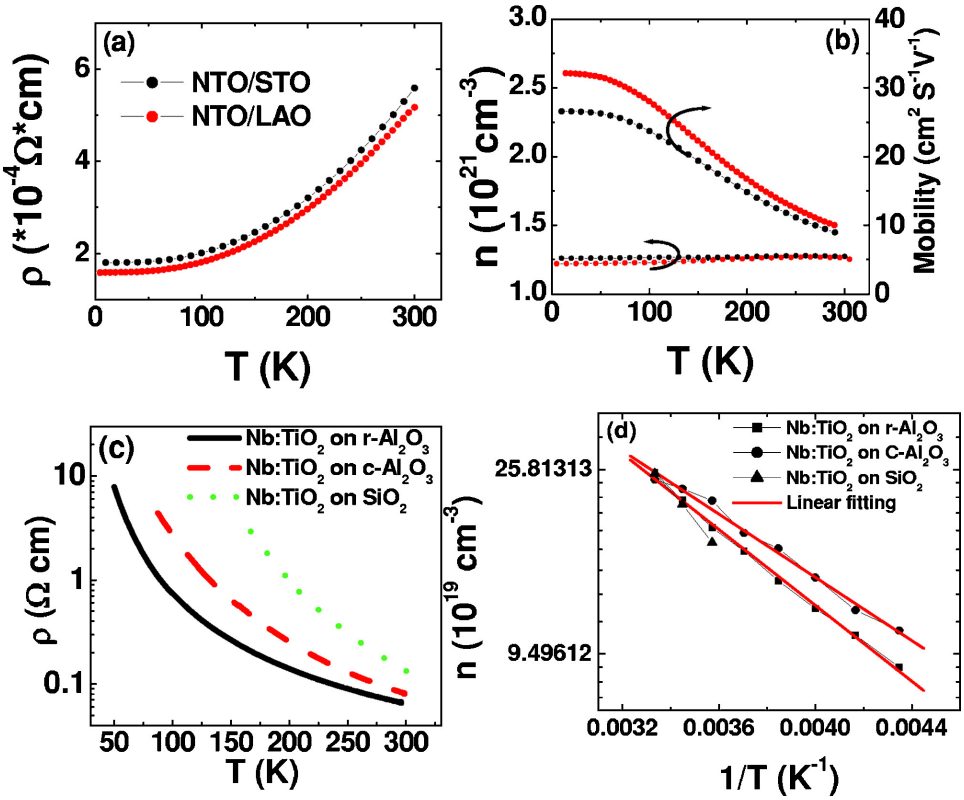

Figure 1.4.2: Transport measurements of anatase and rutile TiO_2 doped with 5% Nb. Resistivity ρ measurements (a) and (c) show the typical behaviour of large (anatase) and small (rutile) polarons respectively. On the right side the Hall measurements in panel (b) and (d) report a constant carrier density n for anatase, whereas that of rutile increases with increases temperature. The plots are reproduced from Zhang *et al.* [36].

move in the crystal [1, 35]. As summarised in Table 1.1, the intensity of the electron-phonon interaction affects the temperature dependence of the mobility. For large polarons, phonon scattering is unlikely and they have an almost free-carrier-like motion, which is characterised by a decreasing mobility with increasing temperature. Small polarons motion occurs instead by phonon-assisted hopping and therefore the mobility increases with increasing temperature. The dynamics of small polarons is described by the Emin-Holstein-Austin-Mott (EHAM) theory, developed in the 1980s [1]. We present the conceptual backbone and main results of the EHAM model in subsection 1.4.2 and the Density Functional Theory (DFT) implementation of it that we used in our calcultion in section 2.5.

An example of different dynamical behaviours of small and large polarons can be ob-

served in the two polimorphs of TiO_2, anatase and rutile. Figure 1.4.2 reports resistivity and Hall measurements conducted on these materials, where the additional charge has been supplied by Nb doping. Anatase shows an increasing resistivity ρ with increasing temperature typical for large polarons, with a constant number of charge carriers n. On the other hand rutile's resistivity decreases with temperature and the carriers number increases, as consequence of higher hopping probability [1].

Since the first experimental observation of polarons in 1963 [35], many types of these quasiparticles have been discovered. They have been classified according to the kind of interactions that favour the polaronic localisation, such as JT polarons and defect polarons. For a complete list of the many cases and a thorough review we remand to [1].

We shall focus in the rest of this work on small polarons, leaving the reader interested in the large ones with [1] and the references therein as a starting point for further investigations.

1.4.1 Ground state energy and band narrowing

In order to go deeper into the physics behind the polaron problem and introduce at least conceptually some of the key quantities that we calculated in our work, we shall present here Holstein's molecular-crystal model [34]. This is a toy model consisting of a single electron in an one-dimensional chain of diatomic molecules, whose orientation and center of gravity are fixed, but whose internuclear separations are allowed to oscillate harmonically. We assume that oscillations at different sites are uncoupled, *i.e.* that the actual optical spectrum is replaced by a single frequency ω (Einstein approximation). Thus we can write the lattice part of the Hamiltonian as

$$H_L = \frac{\omega}{2} \sum_n \left(p_n^2 + q_n^2 \right) \tag{1.25}$$

where q_n is the generalised coordinate describing the oscillation at site n and p_n is the conjugate momentum of q_n. The harmonic oscillator natural units for the lattice coordinates are assumed.

For what concerns the electron, it is assumed that it can be described in a tight-binding approximation, which is the natural framework when we deal with wavefunctions having spatial extension smaller than the lattice constant. We assume thereby that the

interaction between the electron and the lattice can be written as the sum of a rapidly decaying function U centered at each site:

$$V(r, \{q\}) = \sum_n U(r - na, \{q\}) \tag{1.26}$$

the short range condition can hence be expressed as $U(a, \{q\}) \ll U(0, \{q\})$. Therefore, using the second quantisation formalism, the Hamiltonian for our system looks like

$$H = -t \sum_{\langle n,m \rangle} c_n^\dagger c_m + \text{h.c.} + \sum_n [\varepsilon_n(\{q\}) + W_n(\{q\})] c_n^\dagger c_n + \frac{\omega}{2} \sum_n b_n b_n^\dagger \tag{1.27}$$

where $c_n^\dagger$ and c_n are the fermionic creation and annihilation operators at site n, whereas $b_n^\dagger$ and b_n are the bosonic ones. The bosonic vacuum energy has been discarded from the ionic term because it simply introduces an energy shift not relevant in our considerations. The two quantities in the brackets of the second term represent respectively the energy $\varepsilon_n(\{q\})$ of the electron in an isolated molecule and the mean-field contribution $W_n(\{q\})$ to this energy due to the interaction of the electron with the other molecules of the chain.

Following Holstein [34], we assume that W_n can be neglected and that ε_n depends linearly on the ionic coordinate, so that we get eventually

$$H = -t \sum_{\langle n,m \rangle} c_n^\dagger c_m + \text{h.c.} + \frac{\omega}{2} \sum_m b_m b_m^\dagger - g \sum_m n_m \left(b_m^\dagger + b_m \right) \tag{1.28}$$

which is the *Holstein Hamiltonian*. Here n_m is the electronic number operator and $-g$ is the constant that characterises the strength of the electron-phonon interaction. If $W = 4t$ is now the bare bandwidth, we can define a dimensionless coupling constant $\lambda = g^2/\omega W$ and the adiabaticity parameter $\alpha = \omega/t$. The adiabatic limit corresponds to $\alpha \to 0$. In the strong-coupling regime ($\lambda > 1$) characteristic of small polarons, we can apply the Lang-Firsnov transformation (LF) to the Holstein Hamiltonian of Equation 1.28 [37, 38]. In this way, neglecting phonon emission and absorption during the hopping process, we can evaluate the ground state energy of the Holstein Hamiltonian. This approximation consists in taking a zero-phonon state as an ansatz for the ground state:

$$|n\rangle = c_n^\dagger |0\rangle \otimes \prod_m |0_m\rangle \tag{1.29}$$

where $|0_m\rangle$ is the harmonic oscillator ground state at site m. Now, the LF transformation that we want to apply is given by

$$e^S, \quad \text{with} \quad S = \gamma \sum_m n_m \left(b_m^\dagger - b_m\right) \tag{1.30}$$

By means of a formula coming from the famous Baker-Campbell-Hausdorff one (see Proposition 3.35 in [39]), we can easily find the transformed Hamiltonian

$$H = -t \sum_{\langle n,m \rangle} c_n^\dagger c_m \exp\left[\gamma\left(b_m^\dagger - b_m\right) - \gamma\left(b_n^\dagger - b_n\right)\right] + \text{h.c.} + \frac{\omega}{2} \sum_m b_m b_m^\dagger - \frac{g^2}{2\omega} \sum_m n_m \tag{1.31}$$

where the value $\gamma = g/\omega$ has been chosen in order to remove the original electron-phonon term. Calculating the expectation value of this Hamiltonian on Equation 1.29 we get

$$E = -2te^{-g^2/2\omega^2} - \frac{g^2}{2\omega} \tag{1.32}$$

Comparing this expression with the TB energy $-2t$ of a Bloch electron (delocalised solution), we can see that the exponential factor shrinks the bare electronic band, a phenomenon known as *band narrowing*. The second term instead can be identified with the polaron ground state energy E_{pol}: if the electron-phonon coupling is strong enough the kinetic term is completely suppressed and we end up with a bound state with energy $E_{pol} = -g^2/2\omega$.

Even though the Holstein's molecular chain is a toy model, it qualitatively presents some aspects of small polaron physics that we will encounter in the following chapters. In particular the polaron formation energy E_{pol} is accessible in DFT calculation and we will show how it is possible to calculate it in section 2.4.

1.4.2 Polaron hopping

Within Holstein's molecular model described in the previous section, it is possible to make some considerations about the motion of the small polaron [40]. In particular, it is possible to show [40, 41] that this quasiparticles have a mobility

$$\mu \sim \exp\left(-\frac{E_a}{kT}\right) \tag{1.33}$$

at sufficiently high temperature T. Here k is the Boltzmann constant and E_a is the energy barrier for the hopping process, also called activation energy. Without going through all the details of quantitatively precise derivation, we shall introduce the principal argument of the EHAM theory [40], in order to understand how we can calculate the activation energy E_a characteristic of the hopping process.

Let's consider an electron hopping between two molecules. If q_1 and q_2 represent respectively the sole degree of freedom of the first and the second molecule, then their energy Aq_1^2 and Aq_2^2, where A is a constant. By placing an electron at molecule 1 we lower the energy by Bq_1, where B is another constant. Eventually we get a total energy (with respect to a certain zero) for the system given by the molecule plus the electron at site 1 equal to

$$Aq_1^2 - Bq_1 \tag{1.34}$$

which has a minimum $E_1^{min} = -Aq_0^2$ for $q_1 = B/2A \equiv q_0$. We identify this equilibrium situation as a polaron with energy $E_p = Aq_0^2$. Now, if we want the electron to jump from molecule 1 to molecule 2, it is necessary that it has the same energy at both sites

$$-Bq_1 = -Bq_2 \tag{1.35}$$

and therefore the deformation must be the same for the two molecules. To get this configuration we have to add an energy equal to $A(q - q_0)^2$ to the polaron at site 1 and Aq^2 to the molecule at site 2. Overall, the energy that we must provide to the system is

$$W_H = A(q - q_0)^2 + Aq^2 \tag{1.36}$$

which has a minimum $E_a = 0.5E_p$ for $q = 0.5q_0$. Within this simple scheme, E_a represents the activation energy if the process is non-adiabatic. In this case we can neglect the electron's kinetic energy, since it has little chance to hop during a single lattice excitation. On the other hand, in the adiabatic case, the electron goes back and forth several times between the two molecules during each excitation of the lattice. Emin and Holstein [42] calculated that in this case the barrier is lowered by an amount equal to the half bandwidth t of the electron

$$E_a = W_H - t \tag{1.37}$$

These considerations perhaps are more easily seen by introducing a single configurational

coordinate x, such that $q_1 = q_0(x+1)$ and $q_2 = q_0 x$. The energy curves then become

$$E_1 = -E_p + E_p x^2 \tag{1.38a}$$

$$E_2 = -E_p + E_p(x-1)^2 \tag{1.38b}$$

and consist in the two parabolas of Figure 1.4.3. The adiabatic case is represented by the dashed line, which smoothly connects the two minima at $x = 0$ and $x = 1$.

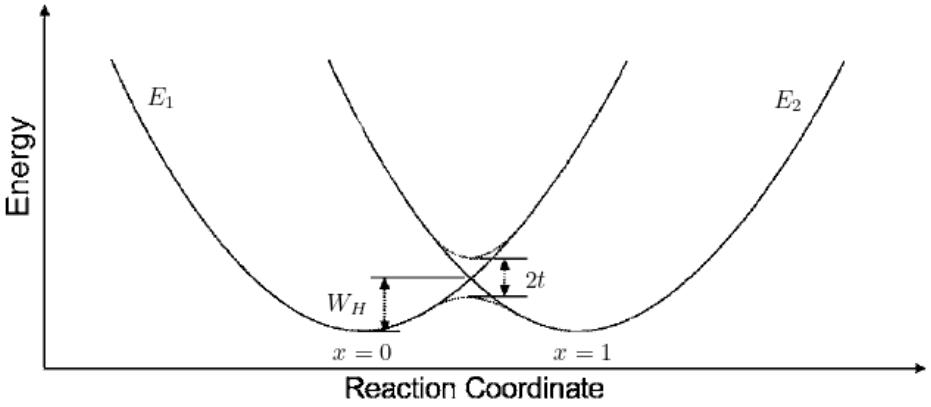

Figure 1.4.3: Energy as a function of the configurational coordinate x. The two parabolas E_1 and E_2 correspond respectively to the electron localised at site 1 and at site 2. The adiabatic regime is represented with a dashed line. The labels show the non-adiabatic hopping barrier W_H and hopping contribution $2t$ that lowers the barrier in the adiabatic case. The picture has been adapted from Deskins and Dupuis [43].

We will talk about the possible ways to evaluate the EHAM hopping barrier in DFT calculations in section 2.5. This quantity can be then compared with values obtained from NMR measurements, like those conducted on lanthanum manganites in [14], and therefore is rather valuable for this work.

Chapter 2

Modelling and methods

Modern computational modelling of materials rely on a variety of techniques, all based on Density Functional Theory (DFT). The range of application of this scheme covers system as different as molecules, nanostructures, solids and surfaces, basically starting from the understanding of the properties of a gas of electrons [44]. Nevertheless, the study of polarons and TMOs requires the development of particular techniques and corrections on top of the standard formulations of DFT, represented by the Local Density Approximation (LDA) or the Generalised Gradient Approximation (GGA) schemes. Especially strong EC and SOC, crucial in our system, require particular care when we want to include them into DFT calculations. This chapter is hence aimed to briefly present DFT and explain the methods we employed, in order to give account for the main physical feature of BNOO with and without the electron doping.

2.1 Density Functional Theory

The first official appearance of DFT dates back to 1964, in a paper [45] published by Pierre Hohehnberg and Walter Kohn, who established the rigorous basis for the development of this theory in the two famous theorems bearing their names (*see* subsection 2.1.2). The first germ of the idea behind DFT is however to be traced back to the works of Llewellyn Thomas [46] and Enrico Fermi [47] in the late 1920s, which we will

immediately summerise in subsection 2.1.1.

If we devote so much attention to this particular theory here is because it turned out to be a real game changer in material modelling, together with the devolopment of calculators powerful enough to bear such kind of simulations. DFT provided us with a tool that has recast the problem of finding the many-body wavefunction $\Psi(x_1, \ldots, x_N)$, describing the electronic ground state in a material, into the drastically simpler search for the electron density $\rho(\mathbf{x})$. Therefore, after presenting DFT's conceptual core, encoded in the Hohenberg-Kohn (HK) theorems, we go down to the self-consistent Kohn-Sham equations (*see* subsection 2.1.3), which are the actual equations implemented in DFT codes, such as VASP. Some words are spent to show where exact results give way to approximations, even though this topic could be and has been treated in whole books.

2.1.1 Prelude: The Thomas-Fermi model

As we said in the introduction to this section on DFT, the Thomas-Fermi model of an electron gas [46–48] is considered the first to shift the attention of the electron density instead of the many-body wavefunction in the search for the system's ground state. So let's see what it is about.

The N electrons of an atom are described by an antisymmetric wavefunction $\Psi(x_1, ..., x_N)$, where $x_i = \mathbf{r}, \sigma_i$ is a shorthand for the position and the spin of the i-th atom, and the Hamiltonian H, which in atomic units looks like

$$H = \sum_{i=1}^{N} \left(-\frac{1}{2}\nabla_i^2 - \frac{Z}{r_i} \right) + \frac{1}{2} \sum_{i \neq j}^{N} \frac{1}{r_{ij}} \tag{2.1}$$

with $r_{ij} = |\mathbf{r}_i - \mathbf{r}_j|$. As soon as the number of electrons is bigger than two, the *electron-electron* interaction term, *i.e* the last on the right hand side of Equation 2.1, makes the Schrödinger problem very difficult and clearly intractable when we consider condensed matter numbers. Thus Thomas and Fermi suggested to use statistical methods in order to approximate the electronic distribution around an atom. Specifically Thomas' assumptions were [46]:

1. in the atom there is an external potential $v(r)$, depending on the distance r from

the nucleus, such that

$$\begin{aligned} v &\to 0 \quad \text{as} \quad r \to \infty, \\ vr &\to 1 \quad \text{as} \quad r \to 0; \end{aligned}$$

2. the electrons are distributed uniformly in the six-dimensional phase space for the motion of an electron at the rate of 2 for each h^3 volume;

3. relativistic corrections can be neglected.

Following [49], we can translate these statements into quantitative expressions. Let's divide the configuration space into cubes of volume $\Delta V = l^3$, each cube contains a free electron gas with ΔN particles. These quantities ΔV and ΔN can have different values in each cube. The electron energy in the box ΔV is

$$\varepsilon = \frac{\pi^2}{2l^2}\left(n_x^2 + n_y^2 + n_z^2\right) \equiv \frac{\pi^2}{2l^2}\, R^2 \tag{2.2}$$

If our boxes are big enough we can adopt the continuum limit and write the number of different states with energy smaller than ε as

$$N(\epsilon < \varepsilon) \simeq \int_0^{\pi/2} \mathrm{d}\varphi \int_0^{\pi} \mathrm{d}\theta \sin\theta \int_0^{\sqrt{2\pi^{-2}l^2\varepsilon}} \mathrm{d}R\; R^2 = \frac{\Delta V (2\varepsilon)^{3/2}}{6\pi^2} \tag{2.3}$$

therefore the number of energy levels between ε and $\varepsilon + \delta\varepsilon$ is

$$g(\varepsilon)\delta\varepsilon = N(\varepsilon + \delta\varepsilon) - N(\varepsilon) = \frac{\Delta V (2\varepsilon)^{1/2}}{2\pi^2}\, \delta\varepsilon \tag{2.4}$$

In order to calculate the total energy ΔE in our cell we need the probability for the state ε to be occupied $f(\varepsilon)$, which is the Fermi-Dirac distribution at zero kelvin, namely a step function. Thus we get

$$\Delta E = 2 \int \mathrm{d}\varepsilon\; g(\varepsilon) f(\varepsilon) \varepsilon = \frac{\Delta V (2\epsilon_F)^{5/2}}{10\pi^2} \tag{2.5}$$

where ϵ_F is the Fermi energy, which is related to the number of occupied state at zero

kelvin as

$$\Delta N = 2 \int \mathrm{d}\varepsilon \; g(\varepsilon) f(\varepsilon) \varepsilon = \frac{\Delta V (2\epsilon_F)^{3/2}}{3\pi^2} \tag{2.6}$$

By combining the previous two equations we can express the total energy of the cell ΔE as a function of the electron density $\rho = \Delta N / \Delta V$:

$$\Delta E = \frac{3}{5} \epsilon_F \Delta N = \frac{\Delta V}{10\pi^2} \big(3\pi^2 \rho\big)^{5/3} \tag{2.7}$$

We can now write the kinetic energy of the free electron gas as the summation of ΔE over all the cubic cells forming the configuration space:

$$T_{TF}[\rho] = C_F \int \mathrm{d}^3 r \; \rho^{5/3}(\mathbf{r}), \quad \text{with} \quad C_F = \frac{3}{10} \big(3\pi^2\big)^{2/3} \simeq 2.87 \tag{2.8}$$

which is a functional of the electron density ρ. By adding the Coulomb repulsion and the electron-electron interaction term, following Thomas' prescriptions, we get the *Thomas-Fermi functional*

$$E_{TF}[\rho] = T_{TF}[\rho] - Z \int \mathrm{d}^3 r \; \frac{\rho(\mathbf{r})}{r} + \frac{1}{2} \int \mathrm{d}^3 r_1 \mathrm{d}^3 r_2 \; \frac{\rho(\mathbf{r}_1)\rho(\mathbf{r}_2)}{|\mathbf{r}_1 - \mathbf{r}_2|} \tag{2.9}$$

We can now apply the variational principle to find the ground state electron density ρ_0 and energy E_0.

The Thomas-Fermi model, as we have presented it here, is a rather simple one. It has the big flaw of not predicting the binding of atoms in molecules and, compared to other methods, it has a lower accuracy [49]. Nonetheless it has the merit of having introduced a shifting in perspective: it allows to determine the ground state of the system using the information stored in the electron density ρ, which lives in the usual configuration space with three coordinates and hence has a clear interpretation, whereas, in the usual Schrödinger picture, we would have had to deal with the $3N$-dimensional wavefunction $\Psi(x_1, ..., x_N)$.

2.1.2 The Hohenberg-Kohn theorems

The 1964 paper by Hohenberg and Kohn [45] shows that the Thomas-Fermi model is an approximation of an exact theory, namely the DFT. Let's rewrite the N-electrons

hamiltonian Equation 2.1 in a more general form

$$H = \sum_{i=1}^{N} \left(-\frac{1}{2}\nabla_i^2 \right) + \frac{1}{2} \sum_{i \neq j}^{N} \frac{1}{r_{ij}} + \sum_{i=1}^{N} v(\mathbf{r}_i) \tag{2.10}$$

where $v(\mathbf{r})$ is an external potential. Then the normalised ground state wavefunction Ψ can be determined by using the variational principle

$$E_0 \leq \langle \Psi | H | \Psi \rangle \tag{2.11}$$

The first HK theorem legitimises the use of the electron density ρ as basic variable, in place of the electron number N and v:

Theorem 2.1.1 (1^{st} Hohenberg-Kohn)**.** *The external potential $v(\mathbf{r})$ is determined, within a trivial additive constant, by the ground state density $\rho(\mathbf{r})$.*

Proof. Let $\rho(\mathbf{r})$ the density for a non-degenerate ground state. Then the number of electrons is trivially given by

$$N = \int \mathrm{d}^3 r \ \rho(\mathbf{r}) \tag{2.12}$$

Now let's assume that v and v' are two external potentials which differ by more than a constant and they both give the same density for the ground state. Thus we have two Hamiltonians H and H' and two corresponding ground state wavefunctions Ψ and Ψ'. We can now write the variational principle for H with Ψ as a trial wavefunction

$$\begin{aligned} E_0 < \langle \Psi' | H | \Psi' \rangle &= \langle \Psi' | H' | \Psi' \rangle + \langle \Psi' | H - H' | \Psi' \rangle \\ &= E_0' + \int \mathrm{d}^3 r \ \rho(\mathbf{r}) [v(\mathbf{r}) - v'(\mathbf{r})] \end{aligned} \tag{2.13}$$

On the other hand the variational principle for H' tells us that

$$\begin{aligned} E_0' < \langle \Psi | H' | \Psi \rangle &= \langle \Psi | H | \Psi \rangle + \langle \Psi | H' - H | \Psi \rangle \\ &= E_0 + \int \mathrm{d}^3 r \ \rho(\mathbf{r}) [v'(\mathbf{r}) - v(\mathbf{r})] \end{aligned} \tag{2.14}$$

By adding these two inequalities we get a contradiction. Therefore, v and v' can differ only for a trivial constant if they provide the same density. □

Let's make explicit the dependence on the external potential of the energy functional:

$$E_v[\rho] = F_{HK}[\rho] + \int \mathrm{d}^3r\ \rho(\mathbf{r})v(\mathbf{r}) \tag{2.15}$$

where $F_{HK}[\rho]$, which contains the kinetic and the electron-electron contribution, is an universal functional in the sense that it does not depend on the external potential. At this point the second theorem of Hohenber and Kohn provides us with a variational principle for the functional $E_v[\rho]$:

Theorem 2.1.2 (2^{nd} Hohenberg-Kohn)**.** *For a trial density $\tilde{\rho}(\mathbf{r})$ such that $\tilde{\rho}(\mathbf{r}) \geq 0$ and $\int \mathrm{d}^3r\ \tilde{\rho}(\mathbf{r}) = N$,*

$$E_0 \leq E_v[\tilde{\rho}] \tag{2.16}$$

where $E_v[\tilde{\rho}]$ is the energy functional of Equation 2.15.

Proof. From the first HK theorem we can say that the trial density $\tilde{\rho}(\mathbf{r})$ determines its own potential, Hamiltonian and wavefunction, respectively $\tilde{v}$, $\tilde{H}$ and $\tilde{\Psi}$. We can use $\tilde{\Psi}$ as a trial wavefunction in the variational principle for H of Equation 2.10:

$$\begin{aligned} E_0 = E_v[\rho] &\leq \left\langle \tilde{\Psi} \middle| H \middle| \tilde{\Psi} \right\rangle \\ &= F_{HK}[\tilde{\rho}] + \int \mathrm{d}^3r\ \tilde{\rho}(\mathbf{r})v(\mathbf{r}) = E_v[\tilde{\rho}] \end{aligned} \tag{2.17}$$

□

Assuming that $E_v[\rho]$ is differentiable and by introducing the Lagrange multiplier μ we can write

$$\delta\left\{ E_v[\rho] - \mu\left[\int \mathrm{d}^3r\ \rho - N \right] \right\} \tag{2.18}$$

which follows from the variational principle Equation 2.16. Thus we have

$$\mu = \frac{\delta E_v[\rho]}{\delta\rho} = v(\mathbf{r}) + \frac{\delta F_{HK}[\rho]}{\delta\rho} \tag{2.19}$$

The Lagrange multiplier μ represents the *chemical potential* of our system and Equation 2.19 constitutes the basic equation of DFT. If we knew the universal functional $F_{HK}[\rho]$, then Equation 2.18 would be an exact equation for the ground state density ρ.

But it turns out that to find an explicit expression for $F_{HK}[\rho]$ is a rather difficult task, which to date no one managed to accomplish. However, numerous approximations for $F_{HK}[\rho]$ have been suggested, but their effectiveness is system dependent, whereas the exact functional would fit to any system. We dedicate the following subsection 2.1.3 to the presentation of the relevant scheme and approximations for this study.

If we now look back at the Thomas-Fermi functional given in Equation 2.9, we recognise that the sum of kinetic term $T_{TF}[\rho]$ and the mean field electron-electron interaction term is just an approximation of $F_{HK}[\rho]$. Indeed, the Thomas-Fermi model can be seen as the first and simplest application of the HK theorems.

The HK theorems, as presented in this section, require an electron density that is *v-representable*, namely a density associated with the antisymmetric wavefunction of the ground state of an Hamiltonian of the form Equation 2.10. However, they can be extended to hold also for more general densities, called *N-representable* densities. Such densities must satisfy the following requirements [49]:

$$\rho(\mathbf{r}) \geq 0 \tag{2.20a}$$

$$\int \mathrm{d}^3 r \ \rho(\mathbf{r}) = N \tag{2.20b}$$

$$\int \mathrm{d}^3 r \ \left|\nabla \rho^{1/2}(\mathbf{r})\right|^2 < \infty \tag{2.20c}$$

Moreover, the requirement of a non-degenerate ground state can be relaxed. For further details we remand to specialised books as [49, 50].

2.1.3 The Kohn-Sham equation

The Thomas-Fermi model simply takes into account the classical coulombic electron-electron interaction

$$J[\rho] = \frac{1}{2} \int \mathrm{d}^3 r \ \mathrm{d}^3 r_1 \ \frac{\rho(\mathbf{r})\rho(\mathbf{r}_1)}{|\mathbf{r} - \mathbf{r}_1|} \tag{2.21}$$

and replace the general kinetic energy functional $T[\rho]$ with that of a non-interacting electrons system. However, to refine this model is not an easy task [49]. A successful approach to incorporate exchange and correlation effects is that of Kohn and Sham [51]. This consists in a mapping of the system of interest into a non-interacting one, in such a way that they are both described by the same ground state density ρ. For N

non-interacting electrons we can write the Hamiltonian as

$$H_s = \sum_{i=1}^{N} \left(-\frac{1}{2}\nabla_i^2 + v_s(\mathbf{r}_i) \right) \tag{2.22}$$

which has the exact ground state described by the Slater determinant

$$\Psi_s = \frac{1}{\sqrt{N!}} \det[\psi_1 \cdots \psi_N] \tag{2.23}$$

where the spin-orbitals ψ_i are the lowest eigenstates of the one-particle Hamiltonian h_s:

$$h_s\psi_i = \left[-\frac{1}{2}\nabla_i^2 + v_s(\mathbf{r}_i) \right] \psi_i = \epsilon_i \psi_i \tag{2.24}$$

Thus the kinetic functional for the non-interacting system is given by

$$T_s[\rho] = \left\langle \Psi_s \middle| \sum_{i=1}^{N} -\frac{1}{2}\nabla^2 \middle| \Psi_s \right\rangle = \sum_{i=1}^{N} \left\langle \Psi_i \middle| -\frac{1}{2}\nabla^2 \middle| \Psi_i \right\rangle \tag{2.25}$$

Even though this mapping requires a non-interacting v-representable density, a formulation with N-representable densities is possible [49].

We can now separate out the non-interacting kinetic energy and the classical part of the coulombic interaction and rewrite the universal functional of the HK theorem as

$$F[\rho] = T[\rho] + V_{ee}[\rho] = T_s[\rho] + J[\rho] + E_{xc}[\rho] \tag{2.26}$$

where $E_{xc}[\rho]$ is called *exchange-correlation* functional and is defined as

$$E_{xc}[\rho] = T[\rho] - T_s[\rho] + V_{ee}[\rho] - J[\rho] \tag{2.27}$$

The non-interacting density can be expressed in terms of the spin-orbitals ψ_i as

$$\rho(\mathbf{r}) = \sum_{i,s} |\psi(\mathbf{r}, s)|^2 \tag{2.28}$$

and we can apply the variational principle of the second HK theorem, performing the variation on the space of spin-orbitals [49]. With a suitable basis we get the self-consistent

Kohn-Sham equation

$$\left[-\frac{1}{2}\nabla^2 + v_{eff}\right]\psi_i = \epsilon_i^{KS}\psi_i \tag{2.29}$$

where the effective potential v_{eff} is given by

$$v_{eff}(\mathbf{r}) = v(\mathbf{r}) + \frac{\delta J[\rho]}{\delta\rho} + \frac{\delta E_{xc}[\rho]}{\delta\rho} = v(\mathbf{r}) + \int \mathrm{d}^3 r_1 \ \frac{\rho(\mathbf{r}_1)}{|\mathbf{r}-\mathbf{r}_1|} + v_{xc}(\mathbf{r}) \tag{2.30}$$

So far the procedure is exact: we can solve Equation 2.29 self-consistently, build the density from Equation 2.28 and eventually get the ground state density from the energy functional. The total energy can be written also as

$$E_0 = \sum_{i=1}^{N} \epsilon_i^{KS} - J[\rho] + E_{xc}[\rho] - \int \mathrm{d}^3 r \ \rho(\mathbf{r}) v_{xc}(\mathbf{r}) \tag{2.31}$$

Thus the total energy is *not* simply the sum of the orbital energies. Nevertheless, there is a theorem by Janak [52] which states that

$$\frac{\partial E}{\partial n_i} = \epsilon_i^{KS} \tag{2.32}$$

where n_i is the occupation of the i-th Kohn-Sham orbital. For what concerns the Kohn-Sham orbitals ψ_i, they have no physical meaning, as their auxiliary nature clearly suggests [49].

However, the exchange-correlation functional $E_{xc}[\rho]$ remains unsettled. The search of an accurate form for $E_{xc}[\rho]$ has encountered tremendous difficulties [49]. The simplest approximation was introduced by the same Khon and Sham and is called *local density approximation* (LDA). They assumed that

$$E_{xc}^{LDA}[\rho] = \int \mathrm{d}^3 r \ \rho(\mathbf{r}) \varepsilon_{xc}[\rho(\mathbf{r})] \tag{2.33}$$

where ε_{xc} is the exchange-correlation energy per particle of a uniform eletron gas with electron density ρ. Basically, we are saying with this formula that the exchange-correlation energy of a non-uniform system can be obtained by applying the uniform electron gas results to an infinitesimal region of the system.

The exchange-correlation energy per particle ε_{xc} can by split into an exchange and a

correlation part as

$$\varepsilon_{xc}(\mathbf{r}) = \varepsilon_x(\mathbf{r}) + \varepsilon_c(\mathbf{r}) \tag{2.34}$$

where the exchange part ε_x can be calculated exactly, whereas the correlation one can be accurately calculated using Monte-Carlo simulations [49].

An improvement to LDA functionals is given by the Generalised Gradient Approximation (GGA), where the exchange-correlation energy per particle depends also on the gradient of the density:

$$E_{xc}^{GGA}[\rho] = \int \mathrm{d}^3 r \; \rho(\mathbf{r})\varepsilon_{xc}[\rho(\mathbf{r}), \boldsymbol{\nabla}\rho(\mathbf{r})] \tag{2.35}$$

2.1.4 Spin Density Functional Theory

The description of magnetic materials requires us to consider spin degree of freedom. In 1973 Rajagopal and Callaway, starting from the Dirac equation, reformulated DFT considering Special Relativity[53]. Indeed, they proved that the ground state total energy of a system of electrons in their ground state is a unique functional of the four current J_μ. We are not so interested in the special form of J_μ in our discussion. Suffice it to say that it contains the electron density ρ, the spin density $\mathbf{s}$ and the electron current [44]. Nowadays, we do not usually take care of electron density in DFT calculation and HK theorems of subsection 2.1.2 are generalised considering the total energy as functional of only ρ and $\mathbf{s}$. If we introduce the density matrix

$$\rho_{\alpha\beta}(\mathbf{r}) = \sum_i^N \psi_i^*(\mathbf{r};\alpha)\psi_i(\mathbf{r};\beta) \tag{2.36}$$

with the greek indices staying for up or down spins, total and spin densities can be written as

$$\rho(\mathbf{r}) = \sum_{\alpha\alpha} \rho_{\alpha\alpha}(\mathbf{r}), \quad \mathbf{s}(\mathbf{r}) = \frac{1}{2}\sum_{\alpha\beta} \rho_{\alpha\beta}(\mathbf{r})\sigma_{\alpha\beta} \tag{2.37}$$

and the variational principle of the second HK theorem can be restated as $E_0 \leq E[\rho_{\alpha\beta}]$. Following the same arguments of subsection 2.1.3, we can write the Kohn-Sham equation

$$\left[-\frac{1}{2}\nabla^2 + v(\mathbf{r}) + v_H(\mathbf{r})\right]\psi_i(\mathbf{r};\alpha) + \sum_\beta v^{XC}_{\alpha\beta}(\mathbf{r})\psi_i(\mathbf{r};\beta) = \epsilon^{KS}_{i,\alpha}\psi_i(\mathbf{r};\alpha) \tag{2.38}$$

where the exchange-correlation potential matrix is given by the functional derivative of E_{xc} with respect to the density matrix. If we define the quantities

$$v_{xc} = \frac{v^{xc}_{11} + v^{xc}_{22}}{2\mu_B}, \quad B^{xc}_x = \frac{v^{xc}_{12} + v^{xc}_{21}}{2\mu_B}, \quad B^{xc}_y = i\frac{v^{xc}_{12} - v^{xc}_{21}}{2\mu_B}, \quad B^{xc}_z = \frac{v^{xc}_{11} - v^{xc}_{22}}{2\mu_B} \tag{2.39}$$

then Kohn-Sham equation can be rewritten as

$$\left[-\frac{1}{2}\nabla^2 + v(\mathbf{r}) + v_H(\mathbf{r}) + v_{xc}(\mathbf{r}) + \mu_B\sigma\cdot\mathbf{B}_{xc}(\mathbf{r})\right]\mathbf{\Psi}_i(\mathbf{r}) = \epsilon_i\mathbf{\Psi}_i(\mathbf{r}) \tag{2.40}$$

where $\mathbf{\Psi}_i$ is the two component spinor defined as

$$\mathbf{\Psi}_i(\mathbf{r}) = \psi_i(\mathbf{r};1)\chi_\uparrow + \psi_i(\mathbf{r};2)\chi_\downarrow \tag{2.41}$$

From Equation 2.40 we can see that when spin degrees of freedom are considered, exchange and correlation effects may give rise to an effective magnetic field $\mathbf{B}_{xc}$. This gives account for magnetic ordering phenomena [44]. Moreover, SOC can be taken into account within this formalism.

The generalisation of the local density approximation expressed in Equation 2.33 to the spin density functional theory is given by

$$E^{LSDA}_{xc}[\rho_{\alpha\beta}] = \int \mathrm{d}^3r\ \rho_{\alpha\beta}(\mathbf{r})\varepsilon^{xc}_{\alpha\beta}[\rho_{\alpha\beta}(\mathbf{r})] \tag{2.42}$$

and in this case we speak about Local Spin-Density Approximation (LSDA).

2.2 The Dudarev's correction

The analysis of TMOs by means of LSDA turned out to by quite unsuccessful, despite the great improvement that this method has brought about for other materials [54–56].

To cite just a couple of examples, it correctly reproduces the magnetic ground state of the NiO-MnO series, but a the same time it predicts materials such as CoO and FeO to be metals, whereas they are known to be insulators. Moreover, the L(S)DA estimation of the band gap of NiO and MnO turns out to be an order of magnitude smaller than experimental values [54].

The main reason for such an inadequacy has to be addressed to the strongly correlated nature of electrons in TM atoms[1] and the fact that in LSDA we consider a local exchange-correlation potential of a non-intercating electron gas. We saw however in section 1.1 that the Hubbard model can describe qualitatively some features of strongly correlated electrons as the Mott Insulator transition. We might expect therefore that adding a Hubbard-like penalty term in the DFT total energy, can lead to more consistent results. This is indeed the case in the Dudarev's scheme [55], where besides the standard LSDA functional, we consider also the effect of the following Hamiltonian:

$$H^U = \frac{U}{2} \sum_{m,m',\sigma} \hat{n}_{m,\sigma} \hat{n}_{m',\sigma} + \frac{U-J}{2} \sum_{m' \neq m,\sigma} \hat{n}_{m,\sigma} \hat{n}_{m',\sigma} \tag{2.43}$$

where the latin indices run over the magnetic quantum numbers ($[-2, 2]$ for d-electrons) and σ gives account for the two spin polarisations. The constant U and J are given by spherically averaged matrix elements of the screened electron-electron interaction. If $E^U[\rho]$ is the energy functional associated with the Hamiltonian in Equation 2.43, we can write a corrected functional as

$$E^{LSDA+U}[\rho] = E^{LSDA}[\rho] + E^U[\rho] - E_{dc}[\rho] \tag{2.44}$$

where $E_{dc}[\rho]$ is called *double counting* functional [57] and it is introduced in order to remove the part of E^U that is supposed to be already included in the LSDA functional. There is no unique choice for $E_{dc}[\rho]$ [58].

Following Dudarev et al. [55], we assume that the double counting term is so that the LSDA+U functional reduces to the standard LSDA one, when there is no orbital

[1] This argument applies for the f-block elements as well.

polarisation, *i.e.* in the atomic limit (integer occupation of the orbitals). Thus

$$\begin{aligned} E_{dc} &= \langle \text{integer } N_\sigma | H^U | \text{integer } N_\sigma \rangle \\ &= \frac{U}{2} \sum_\sigma N_\sigma N_{-\sigma} + \frac{U-J}{2} \sum_\sigma N_\sigma (N_\sigma - 1) \end{aligned} \tag{2.45}$$

where N_σ is the total number of d-electrons with spin projection σ. For integer occupation, we should remember that $n_{m,\sigma}$ is idempotent in order to get the second expression in Equation 2.45. The general case of partial occupations is treated in the Unrestricted Hartree-Fock (UHF) approximation

$$\begin{aligned} E^U &= \langle \text{fractional } N_\sigma | H^U | \text{fractional } N_\sigma \rangle_{UHF} \\ &= \frac{U}{2} \sum_{m,m',\sigma} n_{m,\sigma} n_{m',\sigma} + \frac{U-J}{2} \sum_{m' \neq m,\sigma} n_{m,\sigma} n_{m',\sigma} \end{aligned} \tag{2.46}$$

Therefore, subtracting Equation 2.45 from Equation 2.46 we get the *Dudarev's correction*

$$E^{LSDA+U} = E^{LSDA} + \frac{U-J}{2} \sum_{m,\sigma} n_{m,\sigma} - n_{m,\sigma}^2 \tag{2.47}$$

Notice that here the two integrals U and J enter just as a difference so that we can define $U_{eff} = U - J$, which is the parameter to be set in VASP calculations when the Dudarev's method is selected.

2.3 Constrained magnetic moments

Magnetic materials can show non conventional *non-collinear* configurations usually driven by SOC [2, 6]. In this case the magnetic moments do not lie all on the same direction as in ferro- or antiferromagnets. Because of this peculiar kind of alignment, in the analysis of such materials, it is useful to constrain the direction of the magnetic moments, in order to understand how their energy depends on the canting angle. This can be done in VASP by applying a penalty energy contribution to the total energy which looks like

$$E_p = \lambda \sum_I \left[\mathbf{M}_I - \hat{\mathbf{M}}_I^0 \left(\hat{\mathbf{M}}_I^0 \cdot \mathbf{M}_I \right) \right] \tag{2.48}$$

where the index I runs over all atomic sites, $\hat{\mathbf{M}}_I^0$ is the direction of the magnetic moments as imposed in the input file (INCAR) and $\mathbf{M}_I$ is the integrated magnetic moment for each ion, *i.e.*

$$\mathbf{M}_I = \int_{\Omega_I} \mathrm{d}^3 r \; F_I(|\mathbf{r}|)\mathbf{m}(\mathbf{r}) \tag{2.49}$$

where F_I is a cut-off function, which goes smoothly to zero as it approaches the boundaries of the atomic sphere Ω_I with radius R_I.

The relevant parameters to be set in the calculations are R_I and λ. The former allows a correct integration of the magnetic moments. A good R_I value should be large enough to get a meaningful value of the magnetisation, but, at the same time, too large values would give spurious results, because the integration region would trespass into that of the near ions. On the other hand, the parameter λ controls the strength of the penalty energy and the effectiveness of the constraint. Finely tuned value of λ are required in order to prevent the penalty energy contribution to interfere with the accuracy of the calculations.

2.4 Polarons in DFT

Usually there is no guarantee that DFT+U calculations lead to the correct small polaron ground state [3]. Charge carriers can localise at different sites that could be not equivalent to each other. The resulting different configurations might therefore constitute spurious minima, to which the calculations converge instead of the true ground state. Actually, most of the times, DFT does not predict charge localisation at all and particular strategies must be devised.

First of all, we have to introduce excess charge into the system, this can be accomplished either by putting some kind of defects in the unit cell or by means of some artificial method. For instance, VASP allows to add electrons to the system with a specific flag in the input file, namely NELECT [59]. Accordingly, we should initialise the magnetic moment of the desired site with a value that is $\sim \mu_B$ larger than that of the same site in the pristine material, in order to give account for the spin of the extra electron.

Once excess charge has been introduced, one possibility for inducing the calculation to converge toward a localised solution is to manually perturb the lattice symmetry by

introducing distortions around the desired site, at which we would like to trap the charge. By pushing away the nearest neighbours from the selected site of about 7% the original bond length, the calculations converge into a polaronic solution in most cases. For all calculations in this work, the initial distortions were always between 5% and 10%. Instead of manually perturb the lattice, we can achieve the same goal by chemical substitution: the original atom at the site where charge localisation should occur is substitute with another one that has one electron more. The ionic positions are subsequently let to relax in order to get a tentative structure from which the polaronic solution can be obtained. Since in this work we didn't use chemical substitution in this regard, we remand to [3] for further details. Eventually we can check whether the solution is actually polaronic or not by inspecting the local magnetic moment at the selected site and the ionic distortions around it. The spin of the trapped electron should bring a $\sim \mu_B$ contribution that makes magnetic moment of the polaronic site at least $\sim 0.5\mu_B$ larger than those at other sites. If charge localisation does not take place, on the contrary, the excess charge spreads over many sites and therefore no discernable spin density should appear at any site. From

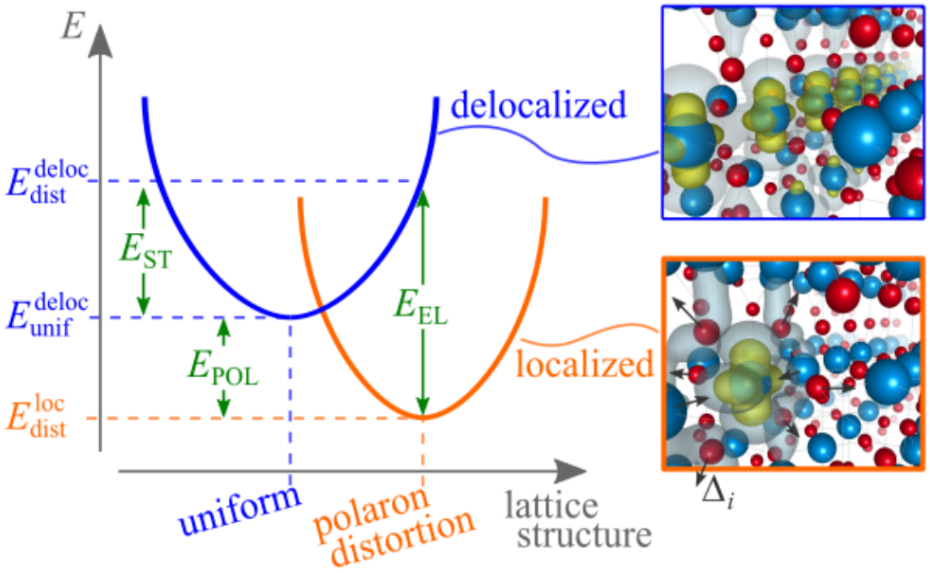

Figure 2.4.1: The picture, taken from Reticcioli *et al.* [3], show the interpretation of the polaron formation energy E_{pol}, the strain energy E_{st} and the electronic gain energy E_{elg}. The lattice on the right is that of rutile TiO_2 of [3].

an electronic point of view, we would find the footprint of the polaron in the Density Of States (DOS) and in the band structure. As we mentioned in section 1.4, small polarons

present themeselves with the formation of in-gap states having almost no dispersion, due to the band narrowing (*see* subsection 1.4.1).

Last but not least, a quantity that usually is readily derivable from DFT calculations is the polaron energy E_{pol} that we introduced in subsection 1.4.1. There is no universally accepted definition for such an energy, but in recent years the one proposed in *e.g.* [1, 3] has been widely adopted in the field. By selectively turning on or off charge localisation, we can define the following energies:

E^{loc}_{dist}: total energy of the system with charge localisation and lattice distortions;

E^{deloc}_{unif}: total energy of the system with delocalised charge carriers and uniform lattice;

E^{deloc}_{dist}: total energy of the system with delocalised charges constrained into the lattice of the polaronic configuration;

which allow us to define also this set of polaronic energies:

$$E_{pol} = E^{loc}_{dist} - E^{deloc}_{unif} \tag{2.50}$$

$$E_{st} = E^{deloc}_{dist} - E^{deloc}_{unif} \tag{2.51}$$

$$E_{elg} = E^{loc}_{dist} - E^{deloc}_{dist} \tag{2.52}$$

whose interpretation is depicted in Figure 2.4.1. The first one, Equation 2.50, is the polaron formation energy and it tells us whether the polaronic solution is more convenient than one with delocalised charge carriers. The strain energy E_{st} represents the structural cost to accomodate the excess charge instead of letting it spread over a uniform lattice. The last one, the electronic gain energy E_{elg}, constitutes the electronic energy gained in the localisation of the carrier via electron-phonon interactions. We can see therefore the polaron formation as the result of two processes of adjustment:

$$E_{pol} = E_{st} + E_{elg} \tag{2.53}$$

that of the lattice and that of the electrons, respectively encoded into E_{st} and E_{elg}.

2.5 Hopping: Linear Interpolation Scheme

In the previous section we considered only polaron ground state properties. However, polarons are characterised by their ability to move around the lattice. It turns out that for small polarons there exist different DFT approaches [3] capable to model, to a certain extent, their dynamics. The simplest one is the Linear Interpolation Scheme (LIS) [3, 43, 60] and it is directly connected to the EHAM theory that we presented in subsection 1.4.2. We choosed it because of its relatively smaller computational cost and more straightforward implementation when compared to *e.g.* the Nudged Elastic Band (NEB) method.

The LIS scheme consists in a sequence of static calculations along a trajectory that connects two polaronic configurations, say one with charge localised at site A and the other one at site B, defined as linear interpolation of the polaronic distortions between the two sites. By introducing the reaction coordinate $x \in [0, 1]$, analogous to the configurational coordinate x of subsection 1.4.2, then this trajectory $q(x)$ is obtained from the ionic coordinates as in configuration A q_A and those as in configuration B q_B as

$$q(x) = q_A + x(q_B - q_A) \tag{2.54}$$

At chosen values of x we perform electronic self-consistent calculations in order to calculate the configuration's energy $E(x)$. With these data it is then possibile to build the adiabatic curve of Figure 1.4.3 and extract the activation energy E_a. In order to obtain the non-adiabatic barrier instead, we have to calculate the two parabolas of Figure 1.4.3 and find their intersection point. This can be done by forcing the charge localistion first say at site A and calculating the total energy for different values of x. Then the same calculations are performed with the charge at site B and eventually the intercept can be evaluated *e.g.* by fitting the two curves [3].

In our case, preliminary NMR measurements suggested that the hopping process is thermally activated and hence adiabatic [43], thereby we applied only the first scheme.

Chapter 3

The Double Perovskite BNCOO

The double perovskite BNOO is characterised by many interesting properties, such as its cAFM ordering accompanied by the Dirac-Mott insulating state. Moreover, X-rays experiments showed that, upon chemical substitution of Na with Ca, the material preserves this relativistic phase instead of undergoing an insulator-metal transition.
We spend in this chapter some words on the properties of these relativistic Osmates, identified by the chemical formula $Ba_2Na_{1-x}Ca_xOsO_6$. *At the same time, we introduce the principal parameter of our* ab-initio *calculations.*

BNOO is a double perovskite with rock-salt ordering of the B cations [7, 9]. It has a face centered cubic (fcc) crystal structure with space group $Fm\overline{3}m$ and lattice constant $a = 8.285\,66(5)$ Å as measured from room temperature powder X-ray diffraction [9]. Figure 3.0.1 shows a $\sqrt{2}a \times \sqrt{2}a \times a$ unit cell rotated by 45° with respect to the c axis and slightly expanded in the ab plane. Yellow and brown octahedra are respectively centered at Na and Os atoms. Oxygen atoms are represented in red and barium in green.

This cell has been chosen instead of the primitive one in order to easily compare the results from the pristine ($x = 0$) and the doped ($x = 0.125$) case, where one Na is substituted with a Ca atom. Moreover, such transformed cell allowed us to easily deal with the canted magnetic moments of BNOO [2], having the cell x-axis along the direction [1 1 0] of the resulting magnetic moment.

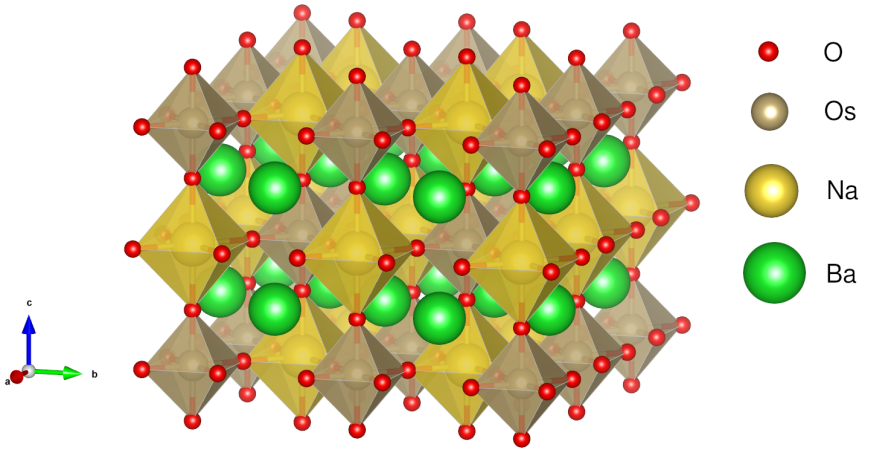

Figure 3.0.1: Super cell of BNOO used in the calculations. The octahedra centered at Na and Os atoms are represented in yellow and brown respectively. O atoms are in red and Ba in green.

By chemically substituting sodium with calcium atoms the unit cell expands according to the Vegard's law. We report the values of the lattice constant as measured in powder X-ray diffraction experiments for different calcium concentrations in Table 3.1, even though we will focus only on the pristine and $x = 0.125$ cases in this work.

3.1 Physical properties of BNOO

BNOO is a heptavalent Os ($5d^1$) compound with unique properties. With one electron per osmium site we would expect BNOO to be a metal, but dc resistivity and infrared reflectivity measurements showed that this is actually an insulator [7]. From first principle calculations, Xiang *et al.* [61] were able to attribute the opening of the insulating gap to the cooperative effect of electron correlation and SOC, making of BNOO a Dirac-Mott Insulator (DMI). Tight-binding analysis allowed to evaluate the hopping matrix element $t \sim 0.05\,\text{eV}$ that couples adjacent octahedra and the Hubbard $U \simeq 3.3\,\text{eV}$ associated with moving an electron from one octahedron to another one [61]. In line with these estimations and the calculations of Fiore Mosca *et al.* [2], we used $U_{eff} = 3.4\,\text{eV}$ in our simulations.

Another peculiar characteristics of BNOO is its magnetic phase. Typically, simple oxides of osmium, such as OsO_2 and $BaOsO_3$, are Pauli paramagnets due to the large

x	a (Å)
0.000	8.285 66(5)
0.125	8.296 93(3)
0.250	8.304 52(3)
0.375	8.318 01(4)
0.500	8.329 85(6)
0.750	8.343 49(3)
0.900	8.352 89(3)
1.000	8.357 80(2)

Table 3.1: Lattice constant a at different Ca concentrations x as measured in room temperature powder X-ray diffraction experiments [9].

spatial extension of the $5d$ orbitals [7]. But more complex oxides, like La_2NaOsO_6 and Ba_2LiOsO_6, appear to show local moment behaviour. Among them, BNOO is the one with the largest magnetic moments ($\sim 0.2\mu_B$) in the ordered phase appearing below $T_c \simeq 6.3\,\mathrm{K}$, which turned out to be an exotic canted anti-ferromagnetic (cAFM) phase with the resulting magnetic moment direct along the [1 1 0] axis [2, 8]. This structure can be understood by looking at Figure 3.1.1. Alternating planes can be identified where the magnetic moments are respectively aligned at a canting angle $+\phi$ and $-\phi$ with respect to the [1 1 0] direction. Let's call 1 and 2 the two inequivalent planes, respectively coloured in blue and red in panels (a) and (c) of Figure 3.1.1. From first principle calculations Fiore Mosca *et al.* [2] obtained for the canting angle $\phi \simeq 67°$. The exotic cAFM pattern appears in BNOO along with staggered JT distortions, represented in panel (b) and (c) of Figure 3.1.1. Osmium octahedra show in fact an overall expansion (Q_1 mode) and tetragonal distortions in the (0 0 1) planes (Q_2 and Q_3 modes): in the blue plane the direction of largest expansion is [1 0 0], whereas in the red one is [0 1 0], as can be understood from panel (c) and (d) of Figure 3.1.1. Notice that these directions do not correspond to those in the computational unit cell of Figure 3.0.1 labelled by the same miller indices. These distortions can be characterised by three of the fifteen generalised coordinates necessary for the O_h symmetry of the octahedral structure, namely Q_1, Q_2

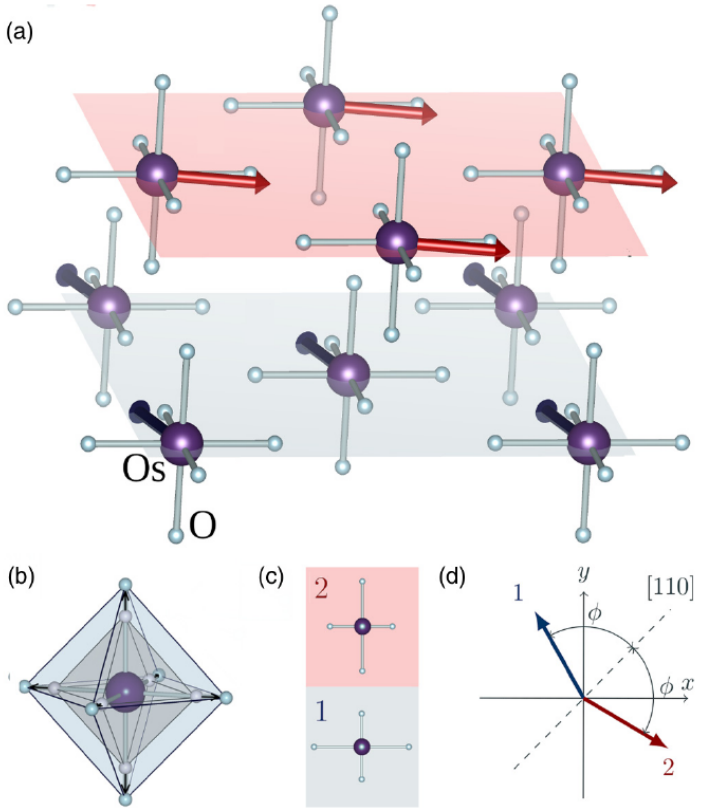

Figure 3.1.1: Magnetic ordering and JT distortions of BNOO. Panels (a) and (d) show the cAFM phase, with canting angle $\phi \simeq 67°$. Panels (b) and (c) clarify the staggered pattern of the JT effect. The figure comes from Fiore Mosca *et al.* [2].

and Q_3. Following Van Vleck [62], these are defined as

$$Q_1 = (X_1 - X_4 + Y_2 - Y_5 + Z_3 - Z_6)/\sqrt{6} \tag{3.1a}$$

$$Q_2 = (X_1 - X_4 - Y_2 + Y_5)/\sqrt{2} \tag{3.1b}$$

$$Q_3 = [X_1 - X_4 + Y_2 - Y_5 - 2(Z_3 - Z_6)]/2\sqrt{3} \tag{3.1c}$$

where X_i, Y_i, Z_i represent the difference in the coordinate of the i-th atom between the distorted and the symmetric structures. The particular labelling takes as first atom the one on the positive x-axis, those on positive y- and positive z-axis follow. The last three are on the negative sides [62]. For BNOO Fiore Mosca *et al.* [2] obtained the values reported in Table 3.2. The variable θ is defined as the arctangent of Q_2/Q_3.

The data in Table 3.2 will be useful later on, when we will look at the polaronic

	Q_1	Q_2	Q_3	θ
plane 1	0.03159	0.00875	0.00164	79.35
plane 2	0.03159	-0.00875	0.00164	-79.35

Table 3.2: Generalised coordinate for the JT distortions in BNOO as calculated by Fiore Mosca *et al.* [2].

distortions, to understand how they modify the original JT pattern observed in the pristine material.

3.2 Chemical substitution: BNCOO

Electrons can be injected into BNOO by chemically substituting sodium with calcium atoms. The so obtained compound $Ba_2Na_{1-x}Ca_xOsO_6$ has been studied by means of first principle calculations, X-ray diffraction and X-ray absorption spectroscopy at different calcium concentrations x by Kesavan *et al.* [9]. When sodium is fully substituted we end up with the double perovskite Ba_2CaOsO_6, where osmium atoms have a formal valence of +6 and the Dirac-Mott gap is still open. This is a rather peculiar fact, considered that the prototypical compound of this class, Sr_2IrO_4, along with $3d$ perovskites, undergoes a MI transition upon doping [9].

Recent results suggest that Ba_2CaOsO_6 presents a ferro-octupolar magnetic ordering [63–66] and therefore a magnetic phase transition has to occur. Moreover, spin-lattice and spin-spin relaxation measurements performed with ^{23}Na NMR spectroscopy showed anomalous peaks recalling those observed in lanthanum manganites, which were associated with a thermally activated SP dynamics [14]. These results have not yet been published but they strongly suggest that a similar process occurs in $Ba_2Na_{1-x}Ca_xOsO_6$ at all Ca concentration between 12.5% and 90% sampled during the experiments. In particular, for the first sample ($x = 0.125$), the experimental team evaluated the activation energy for the hopping process to be $\sim 810\,\mathrm{K}$.

To investigate the robustness of the Dirac-Mott phase and to understand whether the SP-character of the NMR peaks is confirmed by DFT modelling are the main reasons that have motivated this study. In order to test the hypothesis of SP formation upon chemical doping of BNOO, we performed calculations for the pristine and the $x = 0.125$ cases. We will refer to the latter as BNCOO. The results are matter of the next chapter.

Chapter 4

Results

SPs arise from electron-phonon interaction and therefore their footprint can be found in both the electronic and crystal structures. Moreover, they are characterised by being mobile quasiparticles, which can move overcoming an energy barrier, when they are thermally excited. We thereby performed ionic relaxtion calculations to identify the polaronic lattice distortions and, from the instantaneous ground state structure thus obtained, we calculated the electronic density of states and band structure, where SPs appears as in-gap states. Eventually we simulated the SP hopping to evaluate the energy barrier for the dynamical process and compare it with the value estimated from NMR measurements.
We present in this chapter the results produced by our calculations for these quantities, showing at the same time where further investigation is required and from which aspects future works might start.

4.1 Pristine BNOO

As a first step for our calculations, we reproduced the principal results of [2, 9] using the $\sqrt{2}a \times \sqrt{2}a \times a$ supercell of Figure 3.0.1. Having at our disposal the data on the pristine material is useful in order to recognise whther a polaron does form when we employ the conventional doping method (*see* section 2.4). Moreover, they served as a benchmark for the setup of the calculations. Common to them all is the $4 \times 4 \times 6$ k-points grid and the energy cut-off $E_{cut} = 580\,\text{eV}$ for the plane wave basis set. The Perdew-Burke-Ernzerhof

[67] approximation for the exchange-correlation functional has been used throughout this work.

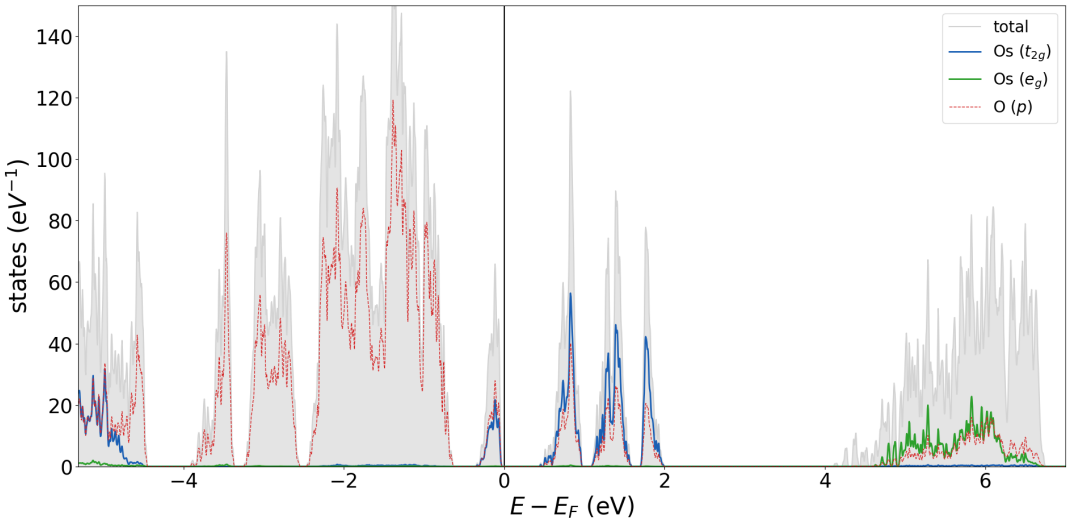

Figure 4.1.1: Density of states of pristine BNOO. The grey shaded area represents the total DOS, whereas the contrbution of the t_{2g} and e_g orbitals of osmium atoms and of the p one of oxygen atoms are drawn respectively in blue, green and red (dashed).

For BNOO we took as lattice constant $a = 8.287\,\text{Å}$ and fixed the magnetic moments to the ground state cAFM ordering, with canting angle $\phi = 67°$, of Fiore Mosca *et al.* [2]. This has been achieved using the constrained magnetic moments flag in VASP and $\lambda = 10$ (*see* section 2.3). As atomic radius for the integration, we took the Wigner-Seitz radius reported in the potential files (POTCARs) [59].

First we let the ionic position to change in order to find the istantaneous ground state configuration. This has been done using a quasi-Newton algorithm [59, 68] with a tolerance of $0.005\,\text{eV/Å}$ for the forces acting on each atom. We thus obtained the JT staggered pattern of section 3.1 reported in Table 4.1. The results are in accordance with those of Fiore Mosca *et al.* [2], also reported in Table 3.2.

	Q_1	Q_2	Q_3	θ
plane 1	0.029	0.011	0.002	78.5
plane 2	0.029	-0.011	0.002	-78.5

Table 4.1: Generalised coordinate for the JT distortions in BNOO.

From the structure obtained after the ionic relaxation, we calculated the DOS re-

ported in Figure 4.1.1. In the plot the osmium t_{2g} and e_g levels along with the p orbital contribution of the oxygen atoms are highlighted with colors. The large overlap of the osmia $5d$ orbitals with the p ones of neighbouring oxygens is clearly visible from the four peaks around the Fermi level. The insulating gap of $\sim 0.50\,\text{eV}$ is opened by EC and SOC as can be seen from the DOS plot reported in [9] and the supplementary materials of [2].

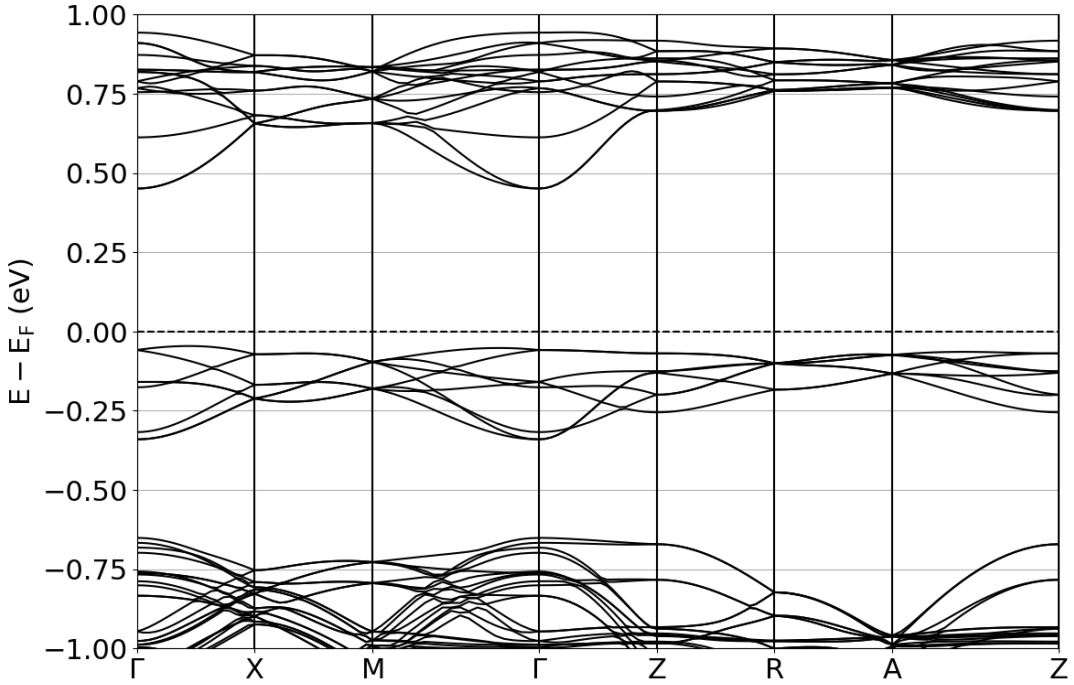

Figure 4.1.2: Band structure of the pristine BNOO supercell. The picture shows a small region of the spectrum around the Fermi energy.

The corresponding bands are reported in Figure 4.1.2, where twenty points have been taken between each pair of high symmetry points. We did not use the band-unfolding technique, which is usually employed in supercell calculations, because of some problems with the software. Therefore, the symmetry points in this plot (and in those of all the subsequent band structures) are to be intended as those of the tetragonal supercell. We referred to [69] for the labelling of the k-space path.

4.2 Conventional doping

For the discussion of polarons it is useful to indroduce labels that identify the osmium atoms in our unit cell. Therefore, we report in Figure 4.2.1 a simplified version of the supercell of Figure 3.0.1 with only the osmium and oxygen atoms, where we numbered the formers starting from those in plane 2. The complete labelling can be read in the figure.

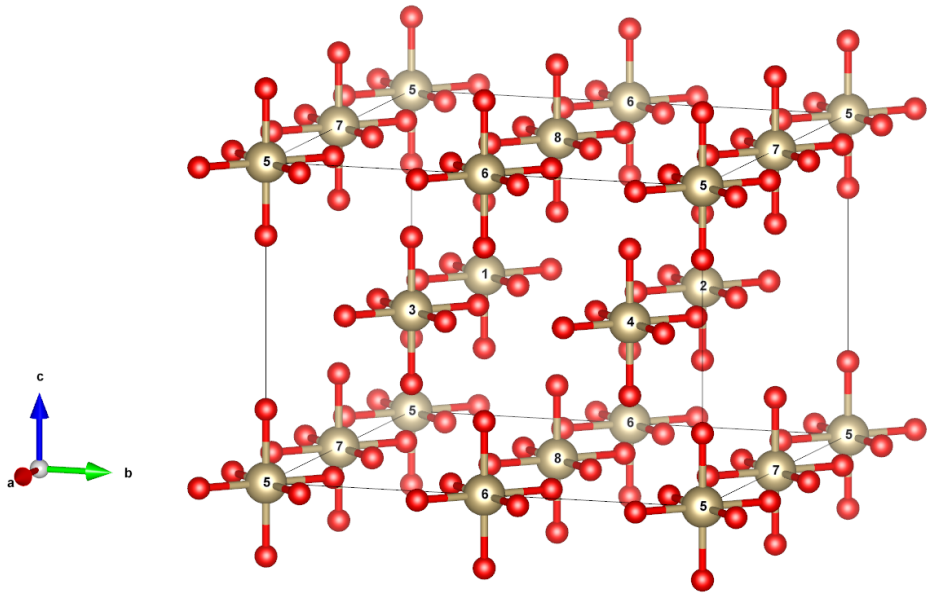

Figure 4.2.1: Unit cell without the Ba and Na atoms. The osmium sites has been numbered starting from plane 2, in order to discuss the polaronic solutions.

We added one excess charge to the system first manually, *i.e.* by inserting an additional electron to the unit cell by means of the flag NELECT available in VASP [59]. The case of chemical doping is analysed later on in section 4.3. In order to trigger localisation we manually distort the lattice around the desired site, as described in section 2.4. Taking as a reference the localisation site, each cartesian coordinate of the neighbouring oxygen atoms has been enlarged by 7% of the original value and then we let the ion positions to relax. We performed this operation at four different sites, two for each magnetically inequivalent plane.

In Table 4.2 we report the distortions of the bonds between osmium and its neighbouring oxygen atoms due to polaron formation. We calculated them with respect to

the structure of the pristine material, including the JT distortions. The reference bond lengths of the OsO_6 octahedra can be read from Table A.1. The results are expressed using the coordinates defined in section 3.1, which means that, for instance, Z_3 refers to the oxygen atom above the osmium and hence lying along the [0 0 1] direction. Since distortions are always smaller than 0.4% but for the octahedron around the localisation site, we characterise here only the structure of the latter in four different cases. A dif-

site	X_1 (%)	X_4 (%)	Y_2 (%)	Y_5 (%)	Z_3 (%)	Z_6 (%)	E_p (meV)
1	2.4	1.7	0.9	0.9	2.2	2.2	113
2	2.1	2.1	0.5	1.2	2.2	2.2	112
7	1.0	1.0	2.0	2.0	2.3	2.3	130
8	0.9	0.9	2.0	2.0	2.3	2.3	132

Table 4.2: Bond length distortions due to polaron formation at different sites as obtained with conventional doping, with respect to the pristine structure. In the last column is reported the polaron energy E_p for each configuration.

ference in total energy of $\sim 20\,\text{meV}$ between the sites lying in the two different planes of Figure 3.1.1 can be noticed from the last column. This unexpected asymmetry may be ascribed to the different deformation of bonds along the same axis, suggesting that more accurate calculations could be necessary. We repeated these structural calculations with the magnetic moments costrained in the directions of the cAFM of pristine BNOO ($\phi = 67°$) but still free to vary their modulus. Also in this case the $\sim 20\,\text{meV}$ is observed between the two planes and thereby we suspect that this asymmetry does not arise from magnetism. For the sites 1 and 2 (plane 2) we can see in Table 4.2 that the distortions in the X_i are about two times bigger than those in the Y_i. This is enough to change the symmetry of the polaronic site that, according to Equation 3.1b, is now characterised by a Q_2 value with opposite sign with respect to the pristine case (compare *e.g* the bond lengths in Table A.1 and Table A.2).

site	Q_1 (Å)	Q_2 (Å)	Q_3 (Å)	θ (°)
1	0.068	0.003	-0.006	153
2	0.068	0.005	-0.006	136
7	0.069	-0.002	-0.007	-167
8	0.069	-0.004	-0.007	-150

Table 4.3: Generalised coordinates for the JT-polaron distortions measured with respect to the symmetric octahedra.

The new values for the generalised coordinate Q_i are reported in Table 4.3, where the bond length distortions are measured with respect to symmetric octahedra having Os−O bond 1.870 Å long. The same happens also for the polaron in plane 1, but with the roles of X_i and Y_i exchanged.

The magnetic moments were allowed to relax from the cAFM pattern of the pristine material (*see* section 3.1). Even though no variations have been observed for the z-

site	m_x (μ_B)	m_y (μ_B)	ϕ (°)
1	0.339	-0.744	-66
2	0.314	-0.754	-67
3	0.314	-0.754	-67
4	0.339	-0.744	-66
5	0.410	0.720	60
6	0.351	0.775	66
7	0.313	0.807	69
8	0.426	1.495	74

Table 4.4: Magnetic moment components in the xy-plane and relative canting angle ϕ for the configuration with the polaron localised at site 8.

component, a slight rotation in the xy plane has occurred, as can be seen from the new values of the canting angle reported in Table 4.4, where the case for the polaron at site 8 is analysed. In particular we can see that, at the polaronic site, the magnetic moment is about two times larger than that at other sites.

The polaron energy E_p reported in Table 4.2 has been calculated from a delocalised solution, obtained adding an electron with NELECT to the structure of the pristine material, *i.e.* without manually distort the lattice around any osmium atom. The density of states and magnetic moment components in the xy-plane are reported respectively in

Figure 4.2.2 and Table 4.5. In this case we can see that the system is metallic and there

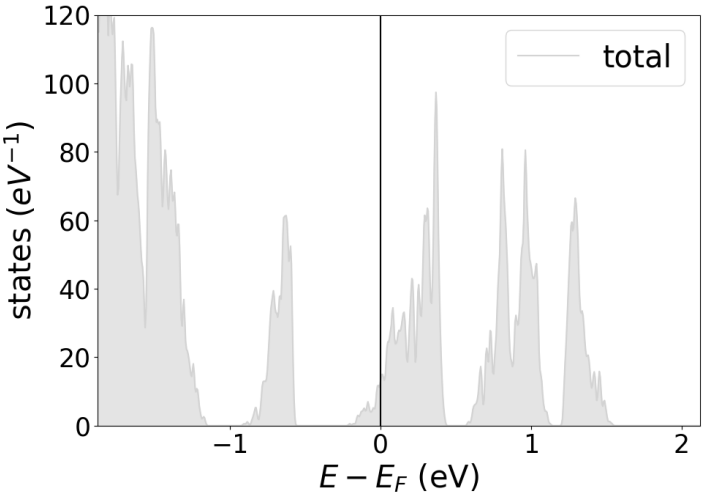

Figure 4.2.2: Density of states for the delocalised solution with NELECT.

site	m_x (μ_B)	m_y (μ_B)
1	0.347	-0.838
2	0.347	-0.838
3	0.347	-0.838
4	0.347	-0.839
5	0.361	0.872
6	0.363	0.872
7	0.358	0.868
8	0.360	0.872

Table 4.5: Non zero magnetic moment components for the delocalised solution with NELECT.

is no magnetic moment significantly larger than the others to signal charge localisation.

On the other hand, when localisation is triggered by manually distorting the lattice, we obtain a DOS as that reported in the bottom panel of Figure 4.2.3 for localisation at site 8, which confirms the formation of a SP-like in-gap state. The blue and red dashed lines in the graph indicate that the major contribution to the polaronic states arises from the t_{2g} orbitals of the osmium at the localisation site and the p-orbitals of its oxygen nearest neighbours. Since the two curves are very similar to each other, we can expect strong $d - p$ hybridisation. The calculated indirect band gap is 0.31 eV.

By inspecting the band structure of the supercell, reported in Figure 4.2.4, we can see that the polaronic feature in the DOS is given by two bands arising from the t_{2g} orbitals of the osmium at the site of localisation. This was somewhat unexpected as usually two in-gap states are characteristic of bipolarons [1, 3], which are bound states of two polarons. If we compare the band structure of Figure 4.2.4 with that of the pristine material in Figure 4.1.2, we can deduce that the lowest polaronic band PB1 has been pulled out from the valence band, wheras the other (PB2) comes from the additional electron, as observed in the other cases of small polaron formation reported in the literature [3]. We confirmed this observation by looking at the total occupacy of

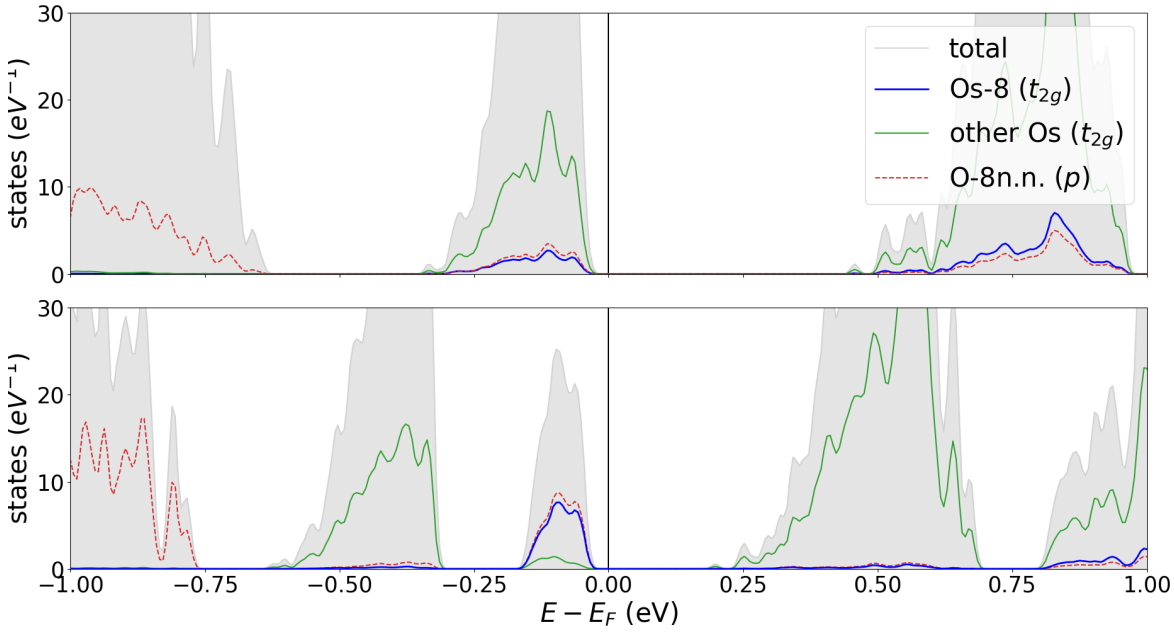

Figure 4.2.3: Density of states of BNOO with one additional electron localised at site 8 (bottom) compared to the pristine one (top). The polaronic peak appears just below the Fermi level and it is mostly due to the t_{2g} levels (blue) of osmium and the p levels of the neighbouring oxygen atoms (red dashed). The contribution of the t_{2g} orbitals of the other osmium atoms is also shown in green.

the osmium 8 t_{2g} orbitals and of the p ones belonging to its neighbouring oxygens. The difference between the pristine and the polaronic solution, excluding the polaronic bands PB1 and PB2, is $\Delta q \simeq 1.1$. If only the osmium t_{2g} orbitals are considered, the same calculation gives $\Delta q \simeq 0.4$, confirming once again the strong $p - d$ hybridisation.

We can further investigated this peculiar electronic structure by looking at the orbital character of the polaronic bands. Table 4.6 shows the Γ-point wavefunction projection onto the lm-projector for $l = 2$ at the polaronic sites. As we did not introduce the Projector Augmented Wave (PAW) implemented in VASP, we remand to [17] for a presentation of this technique and definition of a projector function. As far as we are concerned, this can be understood as a projection onto the Y_{lm} spherical harmonic centered at the desired site. Before we move to this analysis however, some considerations must be done in order to correctly interpret VASP's output. In section 1.3 we gave a definition of t_{2g} and e_g orbitals in a reference frame that was rotate by 45° with respect to that of our calculations. Let's focus on a OsO_6 octahedron. From Figure 4.2.1 we can see that in

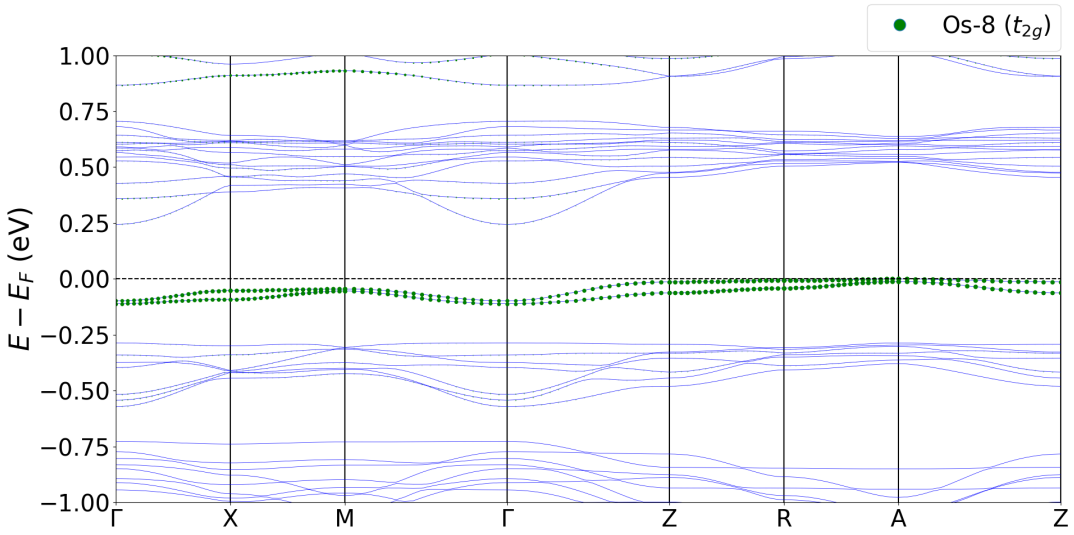

Figure 4.2.4: Band structure of the supercell around the band gap with one electron more added through the NELECT method. The green dots represent the projection onto the t_{2g} orbitals at site 8, where the polaron is localised.

the (0 0 1) plane the oxygen atoms lie on the [1 1 0] and [1 $\bar{1}$ 0] directions, whereas in the theoretical discussion of section 1.3 they were on the [1 0 0] and [0 1 0] directions. If we rotate the wavefunction of Equation 1.22 and Equation 1.23 in order to adapt them to our case, we find out that the d-orbitals transform as

$$\begin{aligned}
|z^2\rangle &\longrightarrow |z'^2\rangle \\
|x^2-y^2\rangle &\longrightarrow -|x'y'\rangle \\
|xy\rangle &\longrightarrow |x'^2-y'^2\rangle \\
|yz\rangle &\longrightarrow \frac{i}{\sqrt{2}}(\,|y'z'\rangle - |x'z'\rangle\,) \\
|xz\rangle &\longrightarrow \frac{i}{\sqrt{2}}(\,|y'z'\rangle + |x'z'\rangle\,)
\end{aligned} \tag{4.1}$$

where we can notice that the 45° rotation exchanges the $|x^2-y^2\rangle$ and $|xy\rangle$ states. Therefore, in the reference frame used by VASP, $|x^2-y^2\rangle$ belongs to the t_{2g} orbitals and $|xy\rangle$ to the e_g ones. We can now recognise in Table 4.6 that the polaronic bands consist of the t_{2g} orbitals of the osmium atom at which the polaron localises. This insight was necessary also to correctly calculate the orbitally projected DOS of Figure 4.1.1 and

Figure 4.2.3. From Table 4.6 we can observe, moreover, that in plane 1 the less en-

site	band	orbital				
		d_{xy}	d_{yz}	d_{z^2}	d_{xz}	$d_{x^2-y^2}$
1	PB1	0.001	0.007	0.000	0.132	0.115
	PB2	0.000	0.224	0.001	0.009	0.021
2	PB1	0.001	0.021	0.000	0.107	0.131
	PB2	0.000	0.206	0.001	0.034	0.007
7	PB1	0.000	0.213	0.001	0.012	0.035
	PB2	0.001	0.022	0.000	0.135	0.095
8	PB1	0.001	0.159	0.001	0.033	0.069
	PB2	0.001	0.077	0.001	0.115	0.061

Table 4.6: Orbital projection of the polaronic bands PB1 and PB2 at the Γ point for different sites. Excess charge introduced with the NELECT method.

ergetic band has a prevalent d_{yz} character, whereas in the more energetic one the d_{xz} contribution is dominant. On the other hand, in plane 2, a reversed condition can be observed.

Eventually we calculated the partial charge distribution associated to the polaronic bands, obtaining Figure 4.2.5, where the yellow isosurface represents the charge density at $1.5 \times 10^{-3}\,\text{Å}^{-3}$. Here we can clearly see that these bands are localised. The relative great amount of charge density on the oxygen atoms around site 8 confirm the strong $p-d$ hybridisation that we observed in the projected DOS of Figure 4.2.3.

4.2.1 Hopping

In order to test whether the SP-model is compatible with the experimental NMR data, we studied the hopping of this quasiparticle between osmium sites using the linear interpolation scheme (LIS) exposed in section 2.5. We report in this work the results for the hopping process taking place between two sites within the same plane, namely that between sites 7 and 8 for plane 1 and that between sites 1 and 2 for plane 2. The interesting case of the hopping between two different planes is currently still under investigation.

We performed a self-consistent electronic relaxation at eight different configurations between those of the polaron fully localised at the starting site and at the final one. Figure 4.2.6 and Figure 4.2.7 show the total energy of the unit cell measured from

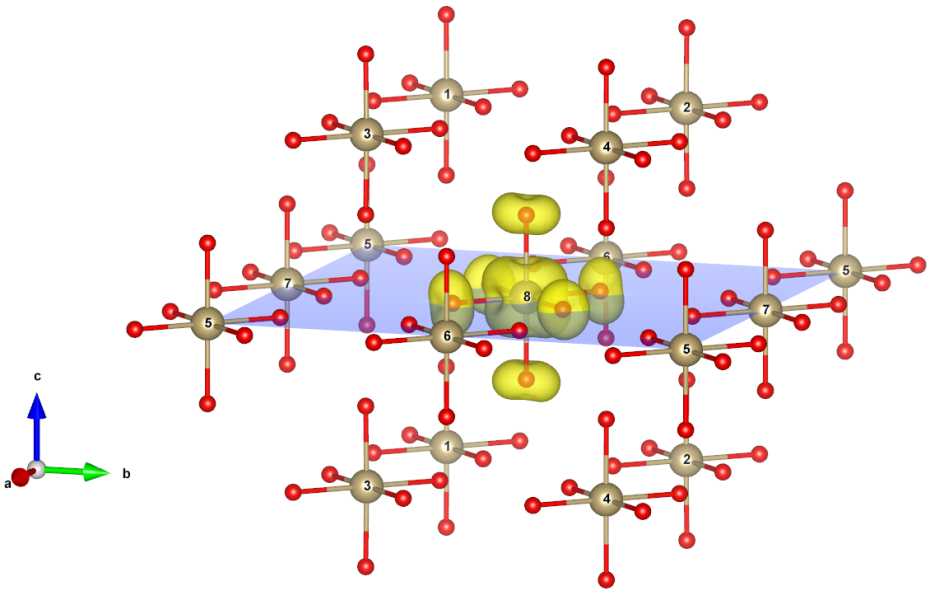

Figure 4.2.5: Charge distribution (yellow) of the polaron localised at site 8 with the NELECT method. This corresponds to the density level $1.5 \times 10^{-3}\,\text{Å}^{-3}$ arising from the two polaronic bands PB1 and PB2 (*see* Figure 4.2.4 and Table 4.6). The blue plane represents plane 1.

that of the starting configuration (first point on the left of the plots) as a function of the reaction coordinate, namely the parameter which interpolates between the two polaronic structures. Both curves are consistent with an adiabatic, thermally activated process, which we would expect from the EHAM theory of subsection 1.4.2. Since the two endpoints have the same energy, we calculated the activation energy $E_a = k_B T_a$ as the difference between the halfway configuration energy (reaction coordinate 0.5) and that of the starting point, obtaining $T_a(1 \to 2) \simeq 603\,\text{K}$ and $T_a(7 \to 8) \simeq 754\,\text{K}$ respectively, close to the experimental value. The difference between these two values, corresponding to $\sim 15\,\text{meV}$, is compatible with that of the polaronic energies seen in Table 4.2: the more stable the polaron, the higher is the energy barrier that it has to overcome in order to hop.

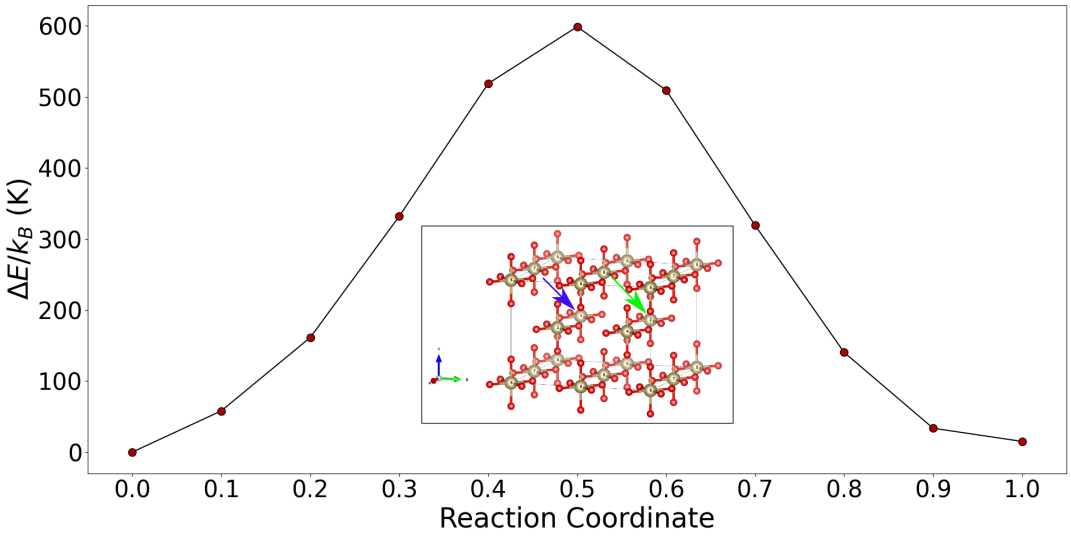

Figure 4.2.6: Total energy as a function of the reaction coordinate for the hopping process between site 1 (inset blue arrow) and site 2 (inset green arrow) in plane 2. Energies are measured from that of the polaron fully localised at site 1. The curve is consitent with that of a thermally activated process with $T_a(1 \to 2) \simeq 603\,\mathrm{K}$.

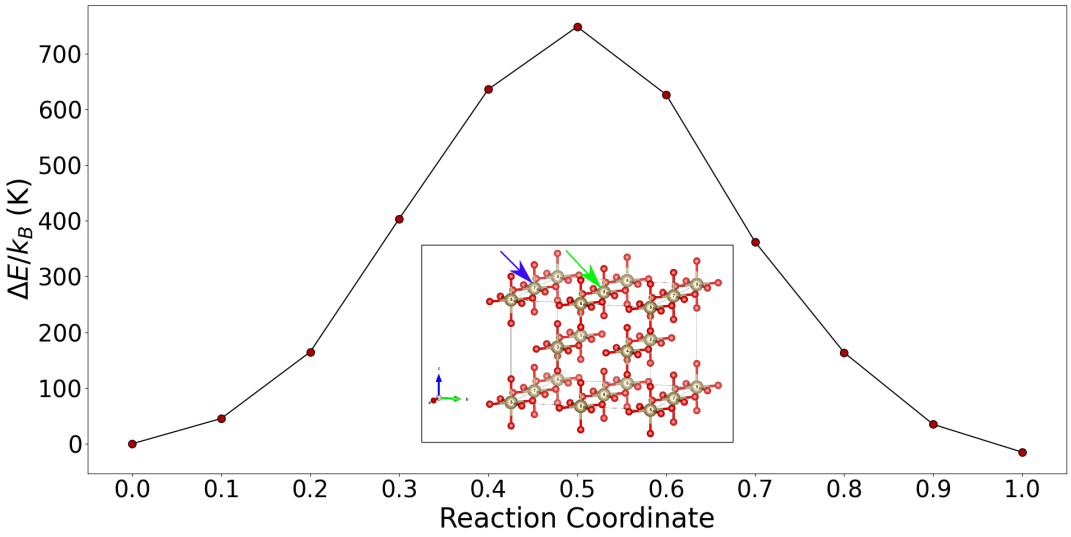

Figure 4.2.7: Total energy as a function of the reaction coordinate for the hopping process between site 7 (inset blue arrow) and site 8 (inset green arrow) in plane 1. Energies are measured from that of the polaron fully localised at site 7. The curve is consitent with that of a thermally activated process with $T_a(7 \to 8) \simeq 754\,\mathrm{K}$.

4.3 Polaron in BNCOO

Charge injection in the double perovskite BNOO can be experimentally realised by substituting Na with Ca atoms. Therefore, it is interesting to go beyond the NELECT method and study polaron formation in $Ba_2Na_{1-x}Ca_xOsO_6$. Nevertheless, due to the complexity of this material, the present work is limited to the analysis of the sample with 12.5% Ca concentration, to which we will refer as BNCOO.

First we add one Ca atom to the unit cell of Figure 3.0.1 and performed a volume relaxation, starting from the lattice constant reported in Table 3.1 for our concentration ($x = 0.125$). Since the unit cell of the pristine material contains eight Na atoms, by substituting just one of them we get the desired concentration. Thus we get a lattice constant $a = 8.294\,\text{Å}$ close to the experimental value. This result required us to choose potentials which include also p-electrons among the valence ones for Na and Ca.

For BNCOO the polaron appeares by itself when we let the ionic position to relax and also when we don't, contrarily to the usual situation encountered in DFT calculations for polaron in $3d$ TMOs. It is useful at this point to report (*see* Figure 4.3.1) osmium atoms arrangement as in Figure 4.2.1 with the added calcium. The spontaneous localisation

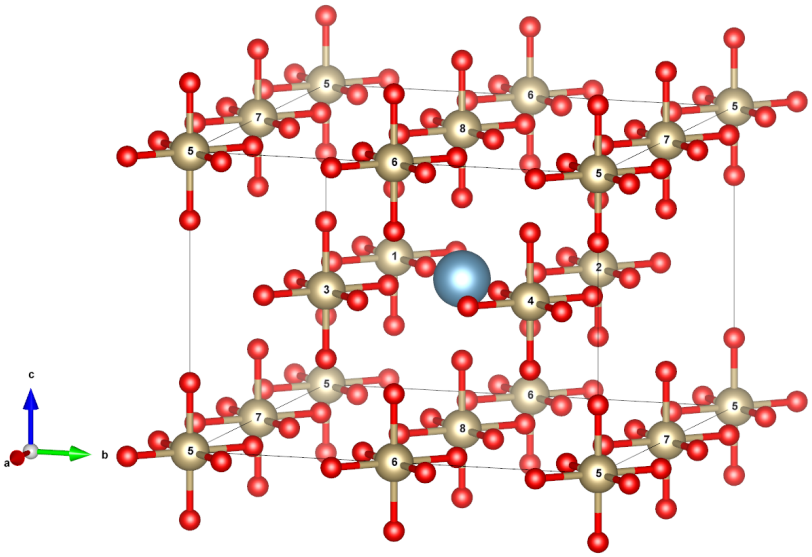

Figure 4.3.1: Simplified unit cell with only the osmium, oxygen and calcium (blue) atoms. The osmium atoms are numbered as in Figure 4.2.1.

occurs at site 8, which is just above (and below) the calcium atom. Nevertheless, in order

to obtain localisation at other sites, manual distortions are required as in the NELECT case.

The automatic trapping causes some trouble when we want to evaluate the polaron energy and a particular strategy must be devised to obtain a delocalised configuration. To overcome this difficulty we used again the flag NELECT, but this time to remove an electron. In this way we could let the ionic lattice to relax and accomodate the new bigger Ca atom, which otherwise attracts the additional electron to its vicinity. We subsequently reintroduced the electron into the relaxed starcture and performed a static self-consistent calculation, which eventually led to a delocalised solution. The DOS and non zero components of the magnetic moments are reported respectively in Figure 4.3.2 and Table 4.7. If we try to relax the ionic position after having reinserted

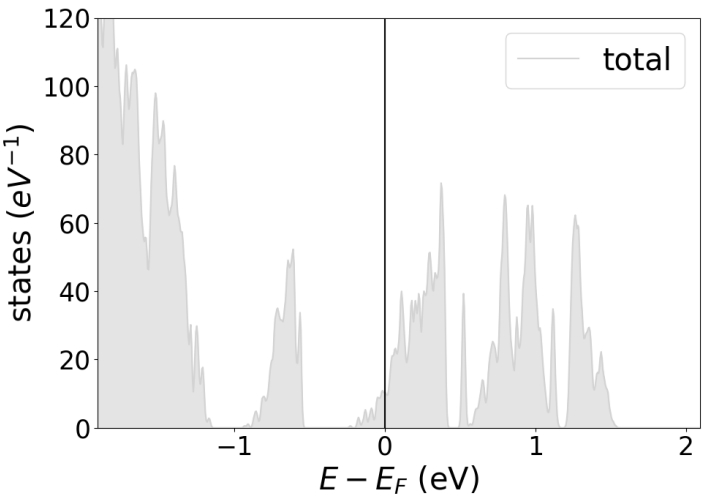

Figure 4.3.2: Density of states for the delocalised solution with $x = 0.125$.

site	m_x (μ_B)	m_y (μ_B)
1	0.343	-0.832
2	0.354	-0.821
3	0.354	-0.821
4	0.343	-0.831
5	0.342	0.804
6	0.359	0.845
7	0.357	0.848
8	0.358	0.844

Table 4.7: Non zero magnetic moment components for the delocalised solution with $x = 0.125$.

the electron, the system converges once again toward the polaronic solution. Since such a relaxation would presumably bring the system toward a lower energy, the (positive) polaron energy E_p that can be obtained from this method, without the final relaxation, is only an upper bound for the real value. We calculated it for the polaron localised at different sites, as can be seen from Table 4.8. The reported values have been obtained without the constraint of the magnetic moments and they show little or no dependence on the distance between the polaronic site and the Ca atom, considering that a difference

of the order of $\sim 10\,\text{meV}$ can depend on the system falling in different non collinear magnetic configurations, which are very close in energy and thereby difficult to probe. Nevertheless, we did not analyse in depth the magnetic behaviour of the polaron in this work. We can also notice that, compared to the NELECT case, the difference of the polaron energies for sites in different plane is disappeared, with the clear exception of site 8. Even for BNCOO, this fact does not depend on whether the magnetic moment directions are constrained or not.

site	distance from Ca (Å)	E_p (meV)
1	4.171	128
2	4.166	123
3	4.166	129
4	4.168	123
5	-	-
6	7.183	129
7	7.183	120
8	4.147	212

Table 4.8: Polaron energy and distance from the calcium atom for the polaron localised at different sites with $x = 0.125$. The values for site 5 are missing do to convergence problems.

It is interesting in this case to look at the distortions of all the osmium octahedra that can be read from Table 4.9 for the polaron localised at site 8. Large variations of

site	X_1 (%)	X_4 (%)	Y_2 (%)	Y_5 (%)	Z_3 (%)	Z_6 (%)
1	1.8	0.4	-0.9	-0.8	-0.3	-0.3
2	-0.1	-0.3	-0.4	1.0	-0.2	-0.2
3	-0.3	-0.1	1.0	-0.4	-0.2	-0.2
4	0.4	1.8	-0.8	-0.9	-0.3	-0.3
5	0.0	0.0	0.2	0.2	-0.2	-0.2
6	-0.1	-0.2	0.4	0.4	-0.1	-0.1
7	-0.2	-0.2	0.4	0.4	0.0	0.0
8	0.4	0.4	1.5	1.5	3.1	3.1

Table 4.9: Bond length distortions due to polaron formation at site 8 and the Ca atom in BNCOO, with respect to the pristine structure.

the bond lengths can be found at the five inequivalent octahedra near the calcium atom

(sites 1, 2, 3, 4 and 8), comparable with those of the polaronic site. They always involve the Os−O bonds pointing toward the calcium atom, making it clear that this defect breaks the original JT symmetry of the neighbouring octahedra. Only site 8 preserves it, even though the sign of Q_2 is inverted as in the NELECT case. This clearly comes from the special position of this site that lies between two Ca atoms. The data presented in Table 4.9 can also be compared with the bond lengths in Table A.8. We report the

site	Q_1 (Å)	Q_2 (Å)	Q_3 (Å)	θ (°)
1	0.066	0.022	0.003	82.9
2	0.065	-0.018	0.001	-86.3
3	0.065	-0.018	0.002	-83.2
4	0.066	0.022	0.001	86.4
5	-	-	-	-
6	0.068	-0.007	-0.006	-132
7	0.068	-0.009	-0.006	-127
8	0.065	-0.002	-0.021	-174

Table 4.10: Generalised coordinates for the polaronic distortions measured with respect to the symmetric octahedra.

values of the generalised coordinate Q_i at the polaronic sites in Table 4.10, measured with respect to symmetric octahedra having Os−O bond length equal to 1.871 Å. In this case, the inversion of Q_2 does not occur for sites 1 and 4 in plane 2. Moreover, by comparing these numbers with those in Table 4.3, we can see that in plane 2 Q_2 is also ~ 10 times bigger with respect to its value for the NELECT polaron. This clearly arises from the large distortions intrduced by the Ca atom.

From the point of view of the electronic structure, the DOS reported in Figure 4.3.3 for the polaron localised at site 8 show the formation of an in-gap peak, typical of small polarons. The contribution of the osmium t_{2g} orbitals and the p ones of the oxygen atoms around the localisation site have been highlighted with colors, which indicate the orbital character of the polaronic feature. As in the NELECT case of Figure 4.2.3, this is mostly due to the t_{2g} orbitals of site 8, which are strongly hybridised with p orbitals of the neighbouring oxygen atoms. The energy gap is in this case equal to 0.32 eV.

Once again the band structure of Figure 4.3.4 reveals that there are two polaronic bands PB1 and PB2.

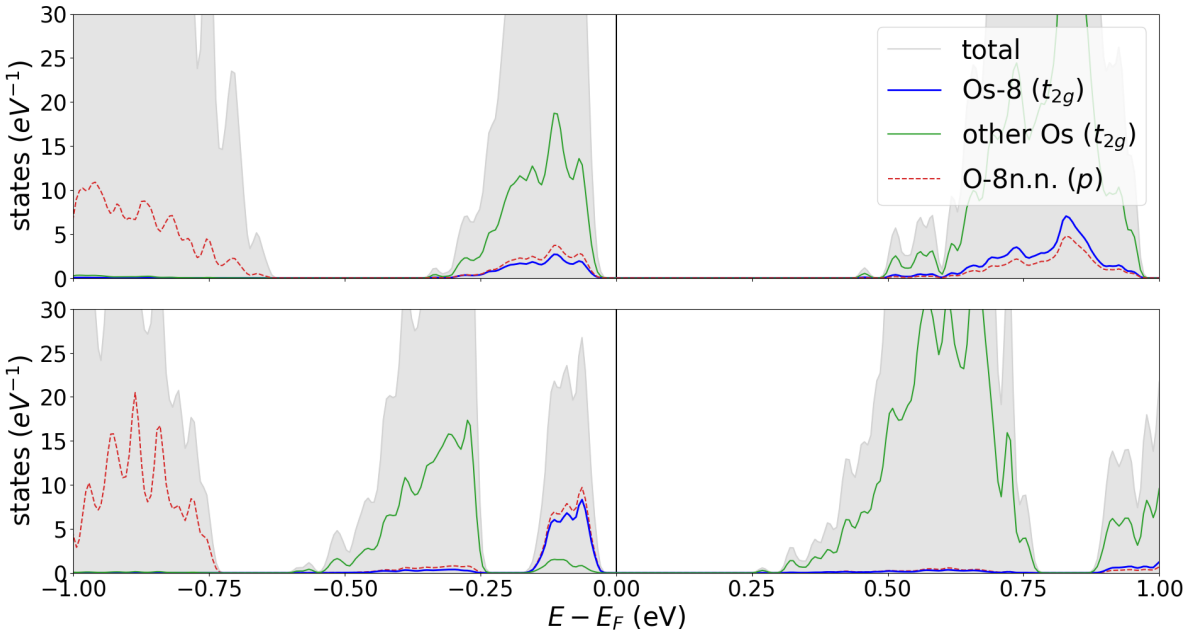

Figure 4.3.3: Density of states of BNCOO with polaron localised at site 8 (bottom) compared to the pristine one (top). The polaronic band appears just below the Fermi level and it is mostly due to the t_{2g} levels (blue) of osmium and the p levels of the neighbouring oxygen atoms (red dashed). The contribution of the t_{2g} orbitals of the other osmium atoms is also shown in green.

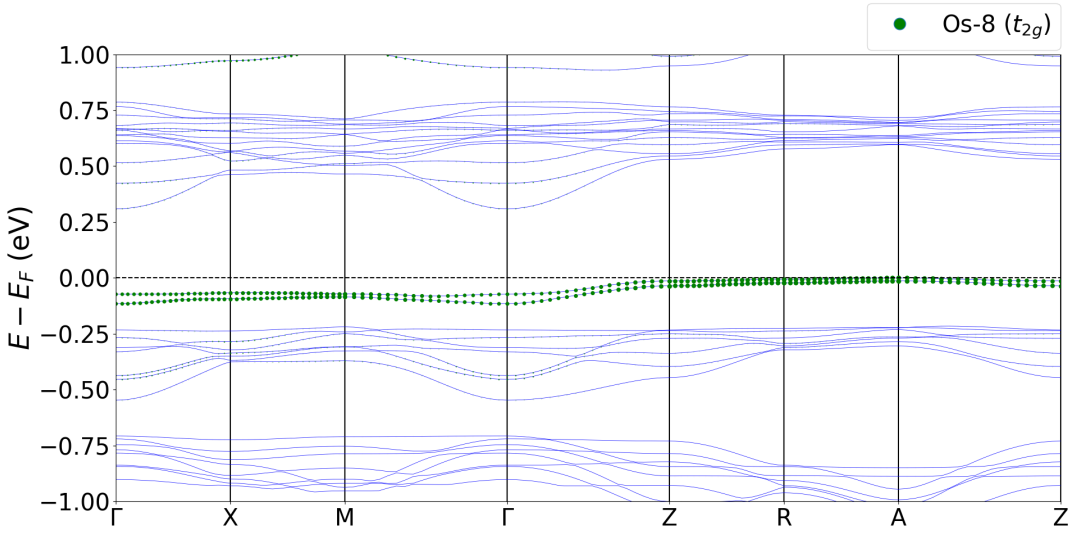

Figure 4.3.4: Band structure of BNCOO supercell with the polaron localised at site 8. The projection onto the t_{2g} orbitals of site 8 is shown with green dots.

By comparing them with those of the NELECT case in Figure 4.2.4, we can see that in BNCOO they appear to be more flat and hence better localised. We can take a look, also in this case, at the orbital occupancies reported Table 4.11. We show only the occupations for the sites also present in Table 4.6 for the NELECT case.

site	band	orbital				
		d_{xy}	d_{yz}	d_{z^2}	d_{xz}	$d_{x^2-y^2}$
1	PB1	0.001	0.000	0.000	0.105	0.158
	PB2	0.000	0.182	0.001	0.035	0.019
2	PB1	0.001	0.014	0.000	0.082	0.148
	PB2	0.000	0.205	0.001	0.033	0.007
8	PB1	0.000	0.256	0.001	0.007	0.010
	PB2	0.001	0.002	0.001	0.167	0.063

Table 4.11: Orbital projection of the polaronic bands PB1 and PB2 at the Γ point for different sites in BNCOO.

It it interesting to notice that the orbital symmetry has not changed much for sites 1 and 2, even though in BNCOO the Ca atom enforces large and asymmetric distortions. But if we recall the asymmetry affecting these sites in the NELECT case, showed in Table 4.2, we can see that it was of the same kind of that arising from the accomodation of Ca in BNCOO. Nevertheless, this seems to be accidental, since we can see no reason behind the bond length difference for oxygen atoms lying on the same axis in the in the symmetric environment of the cell without Ca. For site 8, on the other hand, in each band the d_{xz} and d_{yz} orbitals are less mixed compared to the NELECT case.

For what concerns the hopping process, the simulation in BNCOO presented more difficulties than in the NELECT case, due to the strong tendency of the polaron to localise at site 8. We report the EHAM curve for the hopping occuring in plane 2 in Figure 4.3.5. The evaluation of the energy barrier turns out to give $T_a = 801\,\mathrm{K}$, very close to the value furnished by the NMR experiments.

For the hopping between site 7 and 8 in plane 1, we managed to evaluate only the middle point (reaction coordinate 0.5) with constrained directions of the magnetic moments. In this way we obtained $T_a = 835\,\mathrm{K}$ for the barrier as seen going from site 7 to 8 and $T_a = 1860\,\mathrm{K}$ for the other way round. This asymmetry was to be expected due to the higher E_p at site 8.

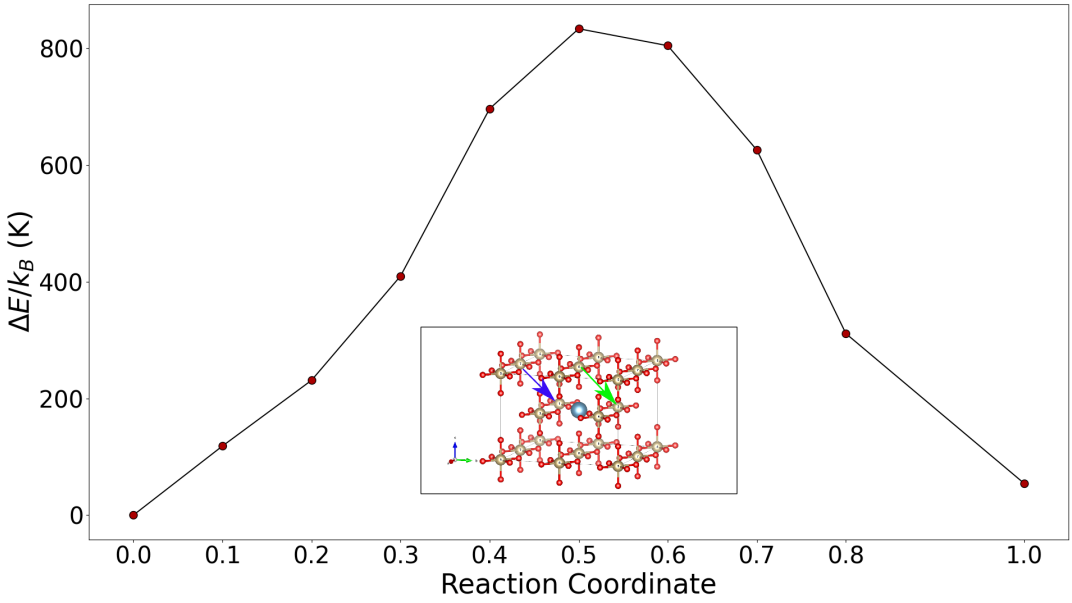

Figure 4.3.5: Total energy as a function of the reaction coordinate for the hopping process between site 1 (inset blue arrow) and site 2 (inset green arrow) in plane 2. Energies are measured from that of the polaron fully localised at site 1. The curve is consitent with that of a thermally activated process with $T_a \simeq 801\,\mathrm{K}$.

Conclusions

The Spin-Orbit coupled double perovskite Ba_2NaOsO_6 (BNOO) presents peculiar properties as it has been proved by both experimental and theoretical works [2, 7–9, 70]. This is a Dirac-Mott Insulator (DMI), whose gap is opened by the interplay of Electronic Correlation (EC) and Spin-Orbit coupling (SOC) interaction. The relativistic insulating phase is moreover followed by an exotic cAFM ordering and a concomitant magnetic moment of $\sim 0.2\mu_B$ per unit formula along the [1 1 0] direction. This magnetic pattern appears toghether with staggered Jahn-Teller (JT) distortions of the osmium octahedra. Among the known DMIs and especially compared to the prototypical Sr_2IrO_4, BNOO has a relatively large EC ($\sim 3\,\text{eV}$) that makes it a possible candidate for Small Polaron (SP) formation in a relativistic background. Very little is indeed known about these quasiparticles in $5d$ Transition Metal Oxides (TMOs), whereas they have been thoroughly studied in the lighter $3d$ ones.

As far as we know, we reported in this work the first numerical evidence of SP formation in such a class of materials. Our first principle calculations, within the GGA+U+SOC scheme, show localised lattice distortions around a single Os atom of about the 2% of the bond lengths in the pristine material. These modifications change in most cases the symmetry of the JT pattern of the pure BNOO, by inverting the sign of the Q_2 coordinate at the polaronic site. The lattice distortions are accompanied by the formation of the typical SP in-gap states in the electronic structure. By inspecting the local magnetic moments and observing the electron density associated with these states, we recognised a localised charge in one of the OsO_6 octahedra.

We studied SP formation first by adding just one electron (NELECT doping) to BNOO and then in the doped osmate $Ba_2Na_{1-x}Ca_xOsO_6$ with 12.5% Ca concentration (BNCOO), where the introduction of a defect brings a further degree of complexity. In both cases we confirmed that the polaronic configuration is more stable than the

delocalised one by calculating the polaron energy E_p. In the NELECT case we got $E_p = 132\,\text{meV}$, whereas in BNCOO the presence of Ca atom hindered the convergence toward a delocalised solution and only the evaluation of an upper bound for E_p was possible. One site is particularly favoured for SP formation where $E_p \lesssim 213\,\text{eV}$, whereas in the other this energy is reduced of about 100 meV. From the band structure with both NELECT and chemical doping we found that the polaronic state is actually composed by two bands, instead of a single one. This turned out to be quite unexpected because usually it is a feature of bipolarons, *i.e* bound states of two polarons [1, 3]. Therefore, a deeper analysis of the character of these states and the processes behind their formation is required.

Another aspect that we didn't analyse but it is crucial for the physics of the doped compound $Ba_2Na_{1-x}Ca_xOsO_6$ is the magnetic phase diagram. The cAFM ordering of pristine BNOO change into an ferro-octupolar one in Ba_2CaOsO_6 [9, 66]. Since the polaron comes with a large magnetic moment ($\sim \mu_B$) compared to those of the osmium atoms, it could play a significant role in such a transition. Besides this, the JT distortions, which have been shown to determine the canted magnetic phase of BNOO, are modified by the SP and therefore a perturbation of this ordering is to be expected. Morevover, the question on which are the precise roles of EC and SOC is yet to be answered. In particular, does the SOC interaction help the SP formation or hinder it?

As a last step, we addressed the problem of SP hopping, both for the NELECT and the chemical doped cases, using the Linear Interpolation Scheme based on the Emin-Holstein-Austin-Mott (EHAM) theory [1, 3, 40, 42]. We analysed this process between two sites lying both in one of the two magnetically inequivalent planes. For both kinds of doping we calculated the energy-reaction coordinate curve, which we found to be consistent with a thermally activated process according to EHAM. Nevertheless, for BNCOO we managed to do so only for the plane containing the Ca atom, due to the limited time and difficulty arising from the preferential localisation in the site above Ca. For the plane without Ca we could only evaluate the energy barrier from the middle point. But without the full curve we cannot decide whether the process is thermally activated, as suggested by the NMR experiments, or mediated by quantum tunneling. Even though this results are still to be refined and completed for the chemically doped case, the estimations for the activation energy that we got (801 K in BNCOO) are in good agreement with the position of the peak observed in NMR experiments at 810 K.

We conclude therefore that our relativistic DFT model confirms the formation of SP in the Spin-Orbit coupled osmate $Ba_2Na_{1-x}Ca_xOsO_6$ and sets out the basis for future investigations at different Ca concentrations and in other $5d$ compounds.

Appendix A

Bond length tables

A.1 pristine BNOO

pristine BNOO						
site	x_1 (Å)	x_4 (Å)	y_2 (Å)	y_5 (Å)	z_3 (Å)	z_6 (Å)
1	1.8861	1.8861	1.9020	1.9020	1.8901	1.8901
2	1.8861	1.8861	1.9020	1.9020	1.8901	1.8901
3	1.8861	1.8861	1.9020	1.9020	1.8901	1.8901
4	1.8861	1.8861	1.9020	1.9020	1.8901	1.8901
5	1.9020	1.9020	1.8861	1.8861	1.8901	1.8901
6	1.9020	1.9020	1.8861	1.8861	1.8901	1.8901
7	1.9019	1.9020	1.8862	1.8861	1.8901	1.8901
8	1.9020	1.9019	1.8862	1.8861	1.8901	1.8901

Table A.1: Bond lengths of the osmium octahedra in pristine BNOO.

A.2 NELECT doping

NELECT polaron at site 1						
site	x_1 (Å)	x_4 (Å)	y_2 (Å)	y_5 (Å)	z_3 (Å)	z_6 (Å)
1	1.9305	1.9173	1.9193	1.9207	1.9315	1.9315
2	1.8978	1.8908	1.9025	1.8974	1.8872	1.8872
3	1.8939	1.8860	1.8996	1.9049	1.8875	1.8875
4	1.8851	1.8828	1.9021	1.9020	1.8929	1.8929
5	1.8837	1.9034	1.8947	1.8942	1.8907	1.8907
6	1.9004	1.9035	1.8940	1.8767	1.8915	1.8915
7	1.8990	1.9043	1.8784	1.8932	1.8912	1.8912
8	1.9049	1.8961	1.8885	1.8859	1.8910	1.8910

Table A.2: Bond lengths of the osmium octahedra with the NELECT polaron at site 1.

NELECT polaron at site 2						
site	x_1 (Å)	x_4 (Å)	y_2 (Å)	y_5 (Å)	z_3 (Å)	z_6 (Å)
1	1.8882	1.8944	1.8999	1.9065	1.8868	1.8868
2	1.9257	1.9254	1.9115	1.9243	1.9314	1.9314
3	1.8818	1.8821	1.9048	1.9056	1.8917	1.8917
4	1.8919	1.8847	1.9005	1.9090	1.8869	1.8869
5	1.9059	1.9061	1.8906	1.8705	1.8923	1.8923
6	1.8928	1.9088	1.8903	1.8867	1.8895	1.8895
7	1.9081	1.8951	1.8904	1.8843	1.8896	1.8896
8	1.9002	1.9016	1.8811	1.8943	1.8903	1.8903

Table A.3: Bond lengths of the osmium octahedra with the NELECT polaron at site 2.

NELECT polaron at site 7						
site	x_1 (Å)	x_4 (Å)	y_2 (Å)	y_5 (Å)	z_3 (Å)	z_6 (Å)
1	1.8910	1.8881	1.9031	1.8945	1.8899	1.8899
2	1.8817	1.8903	1.9005	1.9018	1.8911	1.8911
3	1.8904	1.8816	1.9018	1.9005	1.8911	1.8911
4	1.8880	1.8909	1.8945	1.9031	1.8899	1.8899
5	1.9020	1.9020	1.8903	1.8903	1.8873	1.8873
6	1.9009	1.9010	1.8857	1.8858	1.8909	1.8909
7	1.9207	1.9207	1.9229	1.9230	1.9339	1.9339
8	1.9004	1.9005	1.8936	1.8937	1.8867	1.8867

Table A.4: Bond lengths of the osmium octahedra with the NELECT polaron at site 7.

polaron at site 8						
site	x_1 (Å)	x_4 (Å)	y_2 (Å)	y_5 (Å)	z_3 (Å)	z_6 (Å)
1	1.8830	1.8915	1.8995	1.9012	1.8908	1.8908
2	1.8909	1.8885	1.9022	1.8939	1.8903	1.8903
3	1.8885	1.8909	1.8939	1.9022	1.8903	1.8903
4	1.8915	1.8831	1.9012	1.8995	1.8908	1.8908
5	1.9009	1.9009	1.8858	1.8858	1.8909	1.8909
6	1.9027	1.9027	1.8897	1.8896	1.8874	1.8874
7	1.9008	1.9008	1.8935	1.8935	1.8865	1.8865
8	1.9187	1.9188	1.9245	1.9246	1.9342	1.9342

Table A.5: Bond lengths of the osmium octahedra with the NELECT polaron at site 8.

A.3 Chemical doping

BNCOO polaron at site 2						
site	x_1 (Å)	x_4 (Å)	y_2 (Å)	y_5 (Å)	z_3 (Å)	z_6 (Å)
1	1.9209	1.8886	1.8956	1.9042	1.8760	1.8760
2	1.9212	1.9191	1.8988	1.9513	1.9274	1.9275
3	1.8736	1.8762	1.9300	1.8925	1.8920	1.8920
4	1.8854	1.9175	1.8981	1.9051	1.8764	1.8764
5	1.9089	1.9090	1.8886	1.8689	1.8930	1.8931
6	1.8952	1.9094	1.8903	1.8868	1.8891	1.8891
7	1.9052	1.8930	1.8945	1.8884	1.8904	1.8904
8	1.8835	1.8847	1.8688	1.8808	1.9160	1.9160

Table A.6: Bond lengths of the osmium octahedra with the polaron at site 2 in BNCOO.

BNCOO polaron at site 6						
site	x_1 (Å)	x_4 (Å)	y_2 (Å)	y_5 (Å)	z_3 (Å)	z_6 (Å)
1	1.9213	1.8832	1.8959	1.9047	1.8755	1.8756
2	1.8805	1.8700	1.8908	1.9284	1.8926	1.8926
3	1.8699	1.8806	1.9283	1.8908	1.8926	1.8926
4	1.8832	1.9213	1.9047	1.8959	1.8755	1.8755
5	1.9075	1.9075	1.8897	1.8897	1.8852	1.8852
6	1.9158	1.9158	1.9289	1.9289	1.9364	1.9364
7	1.9014	1.9013	1.8871	1.8871	1.8909	1.8909
8	1.8915	1.8914	1.8691	1.8690	1.9134	1.9134

Table A.7: Bond lengths of the osmium octahedra with the polaron at site 6 in BNCOO.

BNCOO polaron at site 8						
site	x_1 (Å)	x_4 (Å)	y_2 (Å)	y_5 (Å)	z_3 (Å)	z_6 (Å)
1	1.9149	1.8881	1.8973	1.8985	1.8788	1.8788
2	1.8797	1.8773	1.8953	1.9238	1.8887	1.8887
3	1.8773	1.8797	1.9238	1.8954	1.8887	1.8887
4	1.8881	1.9148	1.8985	1.8973	1.8787	1.8787
5	1.9055	1.9055	1.8841	1.8841	1.8895	1.8895
6	1.9045	1.9045	1.8898	1.8898	1.8860	1.8860
7	1.9018	1.9018	1.8914	1.8914	1.8877	1.8877
8	1.9096	1.9096	1.9141	1.9141	1.9501	1.9501

Table A.8: Bond lengths of the osmium octahedra with the polaron at site 8 in BNCOO.

Appendix B

Charge density of the polaronic bands

We report here the charge density of the polaron bands PB1 and PB2 as calculated from the NELECT case.

(a) Top view PB1.

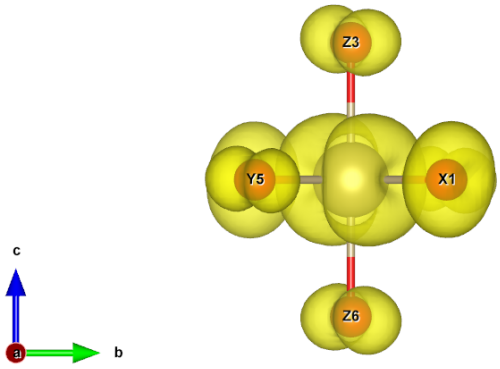

(b) Side view PB1.

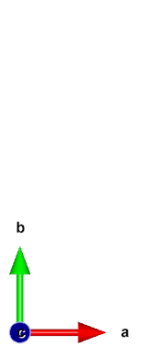

(c) Top view PB2.

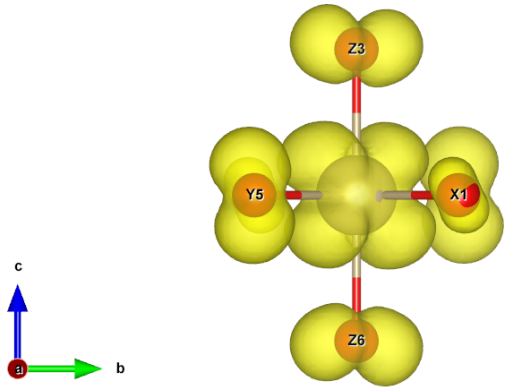

(d) Side view PB2.

Figure B.0.1: The figure shows the isosurface at $1.6 \times 10^{-3}\,\text{Å}^{-3}$ of the charge density of the polaronic bands. In particular, panels (a) and (b) contains respectively the top and the side views for the band PB1, whereas panels (c) and (d) show those for band PB2. The oxygen atoms are labelled according to the convention of section 3.1. In panels (a) and (c) we have X_1, Y_2, X_3, Y_4 ordered anticlockwise, starting from the upper right oxygen (red sphere). At the center there is Z_3. In panels (b) and (d), on the other hand, there are Z_3 (top), Y_5 (middle left), X_1 (middle right) and Z_6 (bottom).

Appendix C

VASP input files

In this appendix we reoport a typical POSCAR and INCAR file used for structural relaxation. The INCARs for static electronic calculation differ only for the missing 'ionic relaxation' section. The lines beginning with # are comments. An explanation of the flags not mentioned in the text can be found at [59].

C.1 Polaron localisation POSCAR

```
BNCOO_localise_at_8
   1.00000000000000
     11.7300526040000008     0.0000000000000000     0.0000000000000000
      0.0000000000000000    11.7300526040000008     0.0000000000000000
      0.0000000000000000     0.0000000000000000     8.2943997399999994
   Na   Ca   Os   Ba   O
     7    1    8   16   48
Selective Dynamics
Direct
  0.0000000000000000  0.0000000000000000  0.5000000000000000  F  F  T
  0.0000000000000000  0.5000000000000000  0.5000000000000000  F  T  T
  0.5000000000000000  0.0000000000000000  0.5000000000000000  T  F  T
  0.2500000000000000  0.2500000000000000  0.0000000000000000  T  T  F
  0.2500000000000000  0.7500000000000000  0.0000000000000000  T  T  F
  0.7500000000000000  0.2500000000000000  0.0000000000000000  T  T  F
```

0.7500000000000000	0.7500000000000000	0.0000000000000000	T	T	F
0.5000000000000000	0.5000000000000000	0.5000000000000000	T	T	T
0.2500000000000000	0.2500000000000000	0.5000000000000000	T	T	T
0.2500000000000000	0.7500000000000000	0.5000000000000000	T	T	T
0.7500000000000000	0.2500000000000000	0.5000000000000000	T	T	T
0.7500000000000000	0.7500000000000000	0.5000000000000000	T	T	T
0.0000000000000000	0.0000000000000000	0.0000000000000000	F	F	F
0.0000000000000000	0.5000000000000000	0.0000000000000000	F	T	F
0.5000000000000000	0.0000000000000000	0.0000000000000000	T	F	F
0.5000000000000000	0.5000000000000000	0.0000000000000000	T	T	F
0.2500000000000000	0.0000000000000000	0.2500000000000000	T	F	T
0.2500000000000000	0.5000000000000000	0.2500000000000000	T	T	T
0.7500000000000000	0.0000000000000000	0.2500000000000000	T	F	T
0.7500000000000000	0.5000000000000000	0.2500000000000000	T	T	T
0.0000000000000000	0.2500000000000000	0.2500000000000000	F	T	T
0.0000000000000000	0.7500000000000000	0.2500000000000000	F	T	T
0.5000000000000000	0.2500000000000000	0.2500000000000000	T	T	T
0.5000000000000000	0.7500000000000000	0.2500000000000000	T	T	T
0.2500000000000000	0.0000000000000000	0.7500000000000000	T	F	T
0.2500000000000000	0.5000000000000000	0.7500000000000000	T	T	T
0.7500000000000000	0.0000000000000000	0.7500000000000000	T	F	T
0.7500000000000000	0.5000000000000000	0.7500000000000000	T	T	T
0.0000000000000000	0.2500000000000000	0.7500000000000000	F	T	T
0.0000000000000000	0.7500000000000000	0.7500000000000000	F	T	T
0.5000000000000000	0.2500000000000000	0.7500000000000000	T	T	T
0.5000000000000000	0.7500000000000000	0.7500000000000000	T	T	T
0.1356302350000007	0.1344814600000035	0.5000012519999970	T	T	T
0.1356302350000007	0.6344814300000010	0.5000012519999970	T	T	T
0.6356302499999984	0.1344814600000035	0.5000012519999970	T	T	T
0.6356302499999984	0.6344814300000010	0.5000012519999970	T	T	T
0.3643697799999970	0.3655185399999965	0.4999987480000030	T	T	T
0.3643697799999970	0.8655185699999990	0.4999987480000030	T	T	T
0.8643697500000016	0.3655185399999965	0.4999987480000030	T	T	T
0.8643697500000016	0.8655185699999990	0.4999987480000030	T	T	T
0.3633339699999993	0.1355583369999991	0.4999982710000026	T	T	T

0.3633339699999993	0.6355583670000016	0.4999982710000026	T	T	T
0.8633339410000005	0.1355583369999991	0.4999982710000026	T	T	T
0.8633339410000005	0.6355583670000016	0.4999982710000026	T	T	T
0.1366660300000007	0.3644416630000009	0.5000017289999974	T	T	T
0.1366660300000007	0.8644416329999984	0.5000017289999974	T	T	T
0.6366660589999995	0.3644416630000009	0.5000017289999974	T	T	T
0.6366660589999995	0.8644416329999984	0.5000017289999974	T	T	T
0.1133339699999993	0.1144416630000009	0.0000000000000000	T	T	F
0.1133339699999993	0.6144416329999984	0.0000000000000000	T	T	F
0.6133339410000005	0.1144416630000009	0.0000000000000000	T	T	F
0.6246699999999999	0.6258899999999999	0.0000000000000000	T	T	F
0.3753300000000000	0.3741100000000000	0.0000000000000000	T	T	F
0.3866660300000007	0.8855583670000016	0.0000000000000000	T	T	F
0.8866660589999995	0.3855583369999991	0.0000000000000000	T	T	F
0.8866660589999995	0.8855583670000016	0.0000000000000000	T	T	F
0.3856302200000030	0.1155185399999965	0.0000000000000000	T	T	F
0.3741900000000000	0.6270700000000000	0.0000000000000000	T	T	F
0.8856302499999984	0.1155185399999965	0.0000000000000000	T	T	F
0.8856302499999984	0.6155185699999990	0.0000000000000000	T	T	F
0.1143697649999993	0.3844814600000035	0.0000000000000000	T	T	F
0.1143697649999993	0.8844814300000010	0.0000000000000000	T	T	F
0.6258100000000000	0.3729300000000000	0.0000000000000000	T	T	F
0.6143697500000016	0.8844814300000010	0.0000000000000000	T	T	F
0.0000000000000000	0.0000000000000000	0.2284899949999968	F	F	T
0.0000000000000000	0.5000000000000000	0.2284899949999968	F	T	T
0.5000000000000000	0.0000000000000000	0.2284899949999968	T	F	T
0.5000000000000000	0.5000000000000000	0.2513400000000000	T	T	T
0.0000000000000000	0.0000000000000000	0.7715100050000032	F	F	T
0.0000000000000000	0.5000000000000000	0.7715100050000032	F	T	T
0.5000000000000000	0.0000000000000000	0.7715100050000032	T	F	T
0.5000000000000000	0.5000000000000000	0.7486600000000000	T	T	T
0.2500000000000000	0.2500000000000000	0.2715100050000032	T	T	T
0.2500000000000000	0.7500000000000000	0.2715100050000032	T	T	T
0.7500000000000000	0.2500000000000000	0.2715100050000032	T	T	T
0.7500000000000000	0.7500000000000000	0.2715100050000032	T	T	T

```
0.2500000000000000  0.2500000000000000  0.7284899949999968  T  T  T
0.2500000000000000  0.7500000000000000  0.7284899949999968  T  T  T
0.7500000000000000  0.2500000000000000  0.7284899949999968  T  T  T
0.7500000000000000  0.7500000000000000  0.7284899949999968  T  T  T
```

C.2 Representative INCAR file

```
SYSTEM = BNCOO_8

# optimisation
NCORE = 24
LREAL = A

# dos
ISMEAR = 0
SIGMA = 0.01
ISYM = -1

# electronic minimisation
ALGO = Fast
ISTART = 0
ENCUT = 580
LMAXMIX = 4

# magnetism
LSORBIT = T

MAGMOM = 24*0.0 0.7815 -1.8410 0.0000
                0.7815 -1.8410 0.0000
                0.7815 -1.8410 0.0000
                0.7815 -1.8410 0.0000
                0.7815  1.8410 0.0000
                0.7815  1.8410 0.0000
                0.7815  1.8410 0.0000
```

```
                                1.1723   2.7615   0.0000  192*0.0
I_CONSTRAINED_M =   1
RWIGS           =   1.164  1.746  1.413  1.979  0.820
LAMBDA          =   10
M_CONSTR        =   24*0.0  0.7815  -1.8410  0.0000
                            0.7815  -1.8410  0.0000
                            0.7815  -1.8410  0.0000
                            0.7815  -1.8410  0.0000
                            0.7815   1.8410  0.0000
                            0.7815   1.8410  0.0000
                            0.7815   1.8410  0.0000
                            0.7815   1.8410  0.0000  192*0.0

# mixing
AMIX      =   0.1
BMIX      =   0.0001
AMIX_MAG  =   0.2
BMIX_MAG  =   0.0001

# Dudarev
LDAU      =   T
LDAUTYPE  =   2
LDAUL     =  -1  -1   2  -1  -1
LDAUU     =   0.0  0.0  3.4  0.0  0.0
LDAUJ     =   0.0  0.0  0.0  0.0  0.0
LDAUPRINT =   2

# ionic relaxation
IBRION =   1
ISIF   =   2
NSW    =   60
EDIFFG =  -0.005

# output
#LPARD  =   T
```

```
#IBAND   =   529
LORBIT   =   11
LORBMOM  =   T
LWAVE    =   T
LCHARG   =   T
```

Bibliography

[1]C. Franchini, M. Reticcioli, M. Setvin, and U. Diebold, "Polarons in materials", Nature Reviews Materials, 1–27 (2021).

[2]D. Fiore Mosca, L. V. Pourovskii, B. H. Kim, P. Liu, S. Sanna, F. Boscherini, S. Khmelevskyi, and C. Franchini, "Interplay between multipolar spin interactions, Jahn-Teller effect, and electronic correlation in a $J_{\text{eff}} = \frac{3}{2}$ insulator", Physical Review B **103**, 104401 (2021).

[3]M. Reticcioli, U. Diebold, G. Kresse, and C. Franchini, "Small Polarons in Transition Metal Oxides", in *Handbook of Materials Modeling: Applications: Current and Emerging Materials*, edited by W. Andreoni and S. Yip (Springer International Publishing, 2019), pp. 1–39.

[4]B. J. Kim, H. Jin, S. J. Moon, J.-Y. Kim, B.-G. Park, C. S. Leem, J. Yu, T. W. Noh, C. Kim, S.-J. Oh, J.-H. Park, V. Durairaj, G. Cao, and E. Rotenberg, "Novel $J_{\text{eff}} = 1/2$ Mott State Induced by Relativistic Spin-Orbit Coupling in Sr_2IrO_4", Physical Review Letters **101**, 076402 (2008).

[5]B. J. Kim, H. Ohsumi, T. Komesu, S. Sakai, T. Morita, H. Takagi, and T. Arima, "Phase-Sensitive Observation of a Spin-Orbital Mott State in Sr_2IrO_4", Science **323**, 1329–1332 (2009).

[6]P. Liu, S. Khmelevskyi, B. Kim, M. Marsman, D. Li, X.-Q. Chen, D. D. Sarma, G. Kresse, and C. Franchini, "Anisotropic magnetic couplings and structure-driven canted to collinear transitions in Sr_2IrO_4 by magnetically constrained noncollinear DFT", Physical Review B **92**, 054428 (2015).

[7]A. S. Erickson, S. Misra, G. J. Miller, R. R. Gupta, Z. Schlesinger, W. A. Harrison, J. M. Kim, and I. R. Fisher, "Ferromagnetism in the Mott Insulator Ba_2NaOsO_6", Physical Review Letters **99**, 016404 (2007).

[8]L. Lu, M. Song, W. Liu, A. P. Reyes, P. Kuhns, H. O. Lee, I. R. Fisher, and V. F. Mitrović, "Magnetism and local symmetry breaking in a Mott insulator with strong spin orbit interactions", Nature Communications **8**, 14407 (2017).

[9]J. K. Kesavan, D. Fiore Mosca, S. Sanna, F. Borgatti, G. Schuck, P. M. Tran, P. M. Woodward, V. F. Mitrović, C. Franchini, and F. Boscherini, "Doping Evolution of the Local Electronic and Structural Properties of the Double Perovskite Ba_2NaOsO_6", The Journal of Physical Chemistry C **124**, 16577–16585 (2020).

[10]P. Liu, M. Reticcioli, B. Kim, A. Continenza, G. Kresse, D. D. Sarma, X.-Q. Chen, and C. Franchini, "Electron and hole doping in the relativistic Mott insulator Sr_2IrO_4: A first-principles study using band unfolding technique", Physical Review B **94**, 195145 (2016).

[11]A. de la Torre, S. McKeown Walker, F. Y. Bruno, S. Riccó, Z. Wang, I. Gutierrez Lezama, G. Scheerer, G. Giriat, D. Jaccard, C. Berthod, T. K. Kim, M. Hoesch, E. C. Hunter, R. S. Perry, A. Tamai, and F. Baumberger, "Collapse of the Mott Gap and Emergence of a Nodal Liquid in Lightly Doped Sr_2IrO_4", Physical Review Letters **115**, 176402 (2015).

[12]Y. Klein and I. Terasaki, "Insight on the electronic state of Sr_2IrO_4 by cationic substitutions", **20**, 295201 (2008).

[13]X. Chen, T. Hogan, D. Walkup, W. Zhou, M. Pokharel, M. Yao, W. Tian, T. Z. Ward, Y. Zhao, D. Parshall, C. Opeil, J. W. Lynn, V. Madhavan, and S. D. Wilson, "Influence of electron doping on the ground state of $(Sr_{1-x}La_x)_2IrO_4$", Physical Review B **92**, 075125 (2015).

[14]G. Allodi, R. De Renzi, and G. Guidi, "^{139}La NMR in lanthanum manganites: Indication of the presence of magnetic polarons from spectra and nuclear relaxations", Physical Review B **57**, 1024–1034 (1998).

[15]G. Kresse and J. Hafner, "Ab initio molecular dynamics for liquid metals", Physical Review B **47**, 558–561 (1993).

[16]G. Kresse and J. Furthmüller, "Efficient iterative schemes for ab initio total-energy calculations using a plane-wave basis set", Physical Review B **54**, 11169–11186 (1996).

[17]P. E. Blöchl, "Projector augmented-wave method", Physical Review B **50**, 17953–17979 (1994).

[18]K. Momma and F. Izumi, "VESTA 3 for three-dimensional visualization of crystal, volumetric and morphology data", Journal of Applied Crystallography **44**, 1272–1276 (2011).

[19]S. P. Ong, W. D. Richards, A. Jain, G. Hautier, M. Kocher, S. Cholia, D. Gunter, V. L. Chevrier, K. A. Persson, and G. Ceder, "Python Materials Genomics (pymatgen): A robust, open-source python library for materials analysis", Computational Materials Science **68**, 314–319 (2013).

[20]D. Khomskii, *Transition Metal Compounds* (Cambridge University Press, 2014).

[21]S. V. Streltsov and D. I. Khomskii, "Jahn-Teller Effect and Spin-Orbit Coupling: Friends or Foes?", Physical Review X **10**, 031043 (2020).

[22]P. Liu and C. Franchini, "Advanced First-Principle Modeling of Relativistic Ruddlesden—Popper Strontium Iridates", Applied Sciences **11**, 2527 (2021).

[23]W. Witczak-Krempa, G. Chen, Y. B. Kim, and L. Balents, "Correlated Quantum Phenomena in the Strong Spin-Orbit Regime", Annual Review of Condensed Matter Physics **5**, 57–82 (2014).

[24]B. Keimer, S. A. Kivelson, M. R. Norman, S. Uchida, and J. Zaanen, "From quantum matter to high-temperature superconductivity in copper oxides", Nature **518**, 179–186 (2015).

[25]Y. Tokura and Y. Tomioka, "Colossal magnetoresistive manganites", Journal of Magnetism and Magnetic Materials **200**, 1–23 (1999).

[26]S. Vasala and M. Karppinen, "A2BBO6 perovskites: A review", Progress in Solid State Chemistry **43**, 1–36 (2015).

[27]N. Ashcroft and N. Mermin, *Solid State Physics* (Cengage Learning, Incorporated, 2021).

[28]B. Bransden and C. Joachain, *Physics of Atoms and Molecules* (Prentice Hall, 2003).

[29]J. B. Goodenough, "Spin-Orbit-Coupling Effects in Transition-Metal Compounds", Physical Review **171**, 466–479 (1968).

[30]H. A. Jahn and E. Teller, "Stability of Polyatomic Molecules in Degenerate Electronic States. I. Orbital Degeneracy", Proceedings of the Royal Society of London Series A **161**, 220–235 (1937).

[31]A. S. Alexandrov and J. T. Devreese, "Continuum Polaron", in *Advances in Polaron Physics*, edited by A. S. Alexandrov and J. T. Devreese, Springer Series in Solid-State Sciences (Springer, 2010), pp. 11–52.

[32]Y. Natanzon, A. Azulay, and Y. Amouyal, "Evaluation of Polaron Transport in Solids from First-principles", Israel Journal of Chemistry **60**, 768–786 (2020).

[33]H. Fröhlich, "Electrons in lattice fields", Advances in Physics **3**, 325–361 (1954).

[34]T. Holstein, "Studies of polaron motion: Part I. The molecular-crystal model", Annals of Physics **8**, 325–342 (1959).

[35]M. Reticcioli, "Polarons on transition-metal oxide surfaces", Doctoral Thesis (University of Vienna, 2018).

[36]S. X. Zhang, D. C. Kundaliya, W. Yu, S. Dhar, S. Y. Young, L. G. Salamanca-Riba, S. B. Ogale, R. D. Vispute, and T. Venkatesan, "Niobium doped TiO_2: Intrinsic transparent metallic anatase versus highly resistive rutile phase", Journal of Applied Physics **102**, 013701 (2007).

[37]M. Hohenadler, "Quantum Monte Carlo and variational approaches to the Holstein model", Physical Review B **69** (2004).

[38]A. S. Alexandrov and J. T. Devreese, "Lattice Polaron", in *Advances in Polaron Physics*, edited by A. S. Alexandrov and J. T. Devreese, Springer Series in Solid-State Sciences (Springer, 2010), pp. 53–95.

[39]B. C. Hall, *Lie groups, Lie algebras, and representations: an elementary introduction*, 2. ed.., Graduate texts in mathematics 222 (Springer, 2015).

[40]I. G. Austin and N. F. Mott, "Polarons in crystalline and non-crystalline materials", Advances in Physics **50**, 757–812 (2001).

[41]T. Holstein, "Studies of Polaron Motion: Part II. The "Small" Polaron", Annals of Physics **281**, 725–773 (2000).

[42]D. Emin and T. Holstein, "Studies of small-polaron motion IV. Adiabatic theory of the Hall effect", Annals of Physics **53**, 439–520 (1969).

[43]N. A. Deskins and M. Dupuis, "Electron transport via polaron hopping in bulk TiO_2: A density functional theory characterization", Physical Review B **75**, 195212 (2007).

[44]F. Giustino, *Materials Modelling using Density Functional Theory: Properties and Predictions* (Oxford University Press, 2014).

[45]P. Hohenberg and W. Kohn, "Inhomogeneous Electron Gas", Physical Review **136**, B864–B871 (1964).

[46]L. H. Thomas, "The calculation of atomic fields", Mathematical Proceedings of the Cambridge Philosophical Society **23**, 542–548 (1927).

[47]E. Fermi, "Un metodo statistico per la determinazione di alcune proprietà dell'atomo", Rendiconti: Accademia Nazionale dei Lincei **6**, 602–607 (1927).

[48]E. Fermi, "Eine statistische Methode zur Bestimmung einiger Eigenschaften des Atoms und ihre Anwendung auf die Theorie des periodischen Systems der Elemente", Zeitschrift für Physik **48**, 73–79 (1928).

[49]R. G. Parr and W. Yang, *Density-Functional Theory of Atoms and Molecules* (Oxford University Press, USA, May 1994).

[50]E. Engel and R. Dreizler, *Density Functional Theory: An Advanced Course*, Theoretical and Mathematical Physics (Springer Berlin Heidelberg, 2011).

[51]W. Kohn and L. J. Sham, "Self-Consistent Equations Including Exchange and Correlation Effects", Physical Review **140**, A1133–A1138 (1965).

[52]J. F. Janak, "Proof that $\frac{\partial E}{\partial n_i} = \epsilon_i$ in density-functional theory", Physical Review B **18**, 7165–7168 (1978).

[53]A. K. Rajagopal and J. Callaway, "Inhomogeneous Electron Gas", Physical Review B **7**, 1912–1919 (1973).

[54]V. I. Anisimov, J. Zaanen, and O. K. Andersen, "Band theory and Mott insulators: Hubbard U instead of Stoner I", Physical Review B **44**, 943–954 (1991).

[55]S. L. Dudarev, G. A. Botton, S. Y. Savrasov, C. J. Humphreys, and A. P. Sutton, "Electron-energy-loss spectra and the structural stability of nickel oxide: An LSDA+U study", Physical Review B **57**, 1505–1509 (1998).

[56]I. V. Solovyev, P. H. Dederichs, and V. I. Anisimov, "Corrected atomic limit in the local-density approximation and the electronic structure of d impurities in Rb", Physical Review B **50**, 16861–16871 (1994).

[57]V. I. Anisimov, F. Aryasetiawan, and A. I. Lichtenstein, "First-principles calculations of the electronic structure and spectra of strongly correlated systems: the LDA+U method", Journal of Physics: Condensed Matter **9**, 767–808 (1997).

[58]S. Ryee and M. J. Han, "The effect of double counting, spin density, and Hund interaction in the different DFT+U functionals", Scientific Reports **8**, 9559 (2018).

[59]*The VASP Manual - Vaspwiki.*

[60]C. W. M. Castleton, A. Lee, and J. Kullgren, "Benchmarking Density Functional Theory Functionals for Polarons in Oxides: Properties of CeO_2", The Journal of Physical Chemistry C **123**, 5164–5175 (2019).

[61]H. J. Xiang and M.-H. Whangbo, "Cooperative effect of electron correlation and spin-orbit coupling on the electronic and magnetic properties of Ba_2NaOsO_6", Physical Review B **75**, 052407 (2007).

[62]J. H. Van Vleck, "The Jahn-Teller Effect and Crystalline Stark Splitting for Clusters of the Form XY6", The Journal of Chemical Physics **7**, 72–84 (1939).

[63]A. Paramekanti, D. D. Maharaj, and B. D. Gaulin, "Octupolar order in d-orbital Mott insulators", Physical Review B **101**, 054439 (2020).

[64]S. Voleti, D. D. Maharaj, B. D. Gaulin, G. Luke, and A. Paramekanti, "Multipolar magnetism in d-orbital systems: Crystal field levels, octupolar order, and orbital loop currents", Physical Review B **101**, 155118 (2020).

[65]S. W. Lovesey and D. D. Khalyavin, "Lone octupole and bulk magnetism in osmate $5d^2$ double perovskites", Physical Review B **102**, 064407 (2020).

[66]L. V. Pourovskii, D. F. Mosca, and C. Franchini, "Ferro-octupolar order and low-energy excitations in d^2 double perovskites of Osmium", arXiv:2107.04493 [cond-mat] (2021).

[67]J. P. Perdew, K. Burke, and M. Ernzerhof, "Generalized Gradient Approximation Made Simple", Physical Review Letters **77**, 3865–3868 (1996).

[68]P. Pulay, "Convergence acceleration of iterative sequences. the case of scf iteration", Chemical Physics Letters **73**, 393–398 (1980).

[69]W. Setyawan and S. Curtarolo, "High-throughput electronic band structure calculations: Challenges and tools", Computational Materials Science **49**, 299–312 (2010).

[70]K.-W. Lee and W. E. Pickett, "Orbital-quenching–induced magnetism in Ba_2NaOsO_6", Europhysics Letters (EPL) **80**, 37008 (2007).